AD-A260 015

PL-TR-92-2073

PRECIPITATING AURORAL ELECTRON FLUX CHARACTERISTICS BASED ON UV DATA OBTAINED BY THE AIRS EXPERIMENT ONBOARD THE POLAR BEAR SATELLITE

D. J. Strickland
R. J. Cox

DTIC
S ELECTE
DEC 3 0 1992
A D

Computational Physics, Inc.
2750 Prosperity Avenue
Suite 600
Fairfax, VA 22031

March, 1992

Final Repcrt
Period Covered: August, 1988 - July, 1991

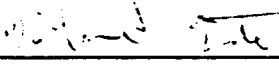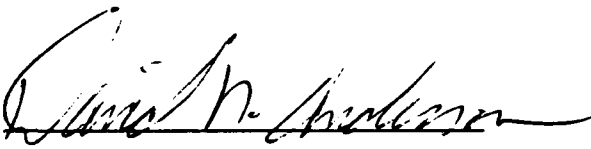PHILLIPS LABORATORY
AIR FORCE SYSTEMS COMMAND
HANSCOM AIR FORCE BASE MASSACHUSETTS 01731-5000

92 12 28 125

This technical report has been reviewed and is approved for publication.

RICHARD EASTES
Contract Manager

DAVID ANDERSON
Branch Chief

WILLIAM K. VICKERY
Division Director

REPORT DOCUMENTATION PAGE

Pub c reporting burden for this collection of information is estimated to average 1 hour per response, including the time for reviewing instructions, searching existing data sources, gathering and maintaining the data needed, and completing and reviewing the collection of information. Send comments regarding this burden estimate or any other aspect of this collection of information, including suggestions for reducing this burden, to Washington Headquarters Services, Directorate for Information Operations and Reports, 1215 Jefferson Davis Highway, Suite 1204, Arlington, VA 22202-4302, and to the Office of Management and Budget, Paperwork Reduction Project (0704-0188), Washington, DC 20503.

1. AGENCY USE ONLY (Leave blank)	2. REPORT DATE March 1992	3. REPORT TYPE AND DATES COVERED Final Report (Aug 1988–July 1991)

4. TITLE AND SUBTITLE
Precipitating Auroral Electron Flux characteristics
Based on UV Data Obtained by the Airs Experiment
Onboard the Polar Bear Satellite

5. FUNDING NUMBERS
PE 62101F
PR 4643 TA 11 WU AF
Contract F19628-88-C-0113

6. AUTHOR(S)
D. J. Strickland
R. J. Cox

7. PERFORMING ORGANIZATION NAME(S) AND ADDRESS(ES)
Computational Physics, Inc
2750 Prosperity Avenue, Suite 600
Fairfax, VA 22031

8. PERFORMING ORGANIZATION REPORT NUMBER

9. SPONSORING/MONITORING AGENCY NAME(S) AND ADDRESS(ES)
Phillips Laboratory
Hanscom AFB, MA 01731-5000

Contract Manager: Richard Eastes/GPIM

10. SPONSORING/MONITORING AGENCY REPORT NUMBER

PL-TR-92-2073

11. SUPPLEMENTARY NOTES

12a. DISTRIBUTION/AVAILABILITY STATEMENT

Approved for public release; distribution unlimited

12b. DISTRIBUTION CODE

13. ABSTRACT (Maximum 200 words)

The AIRS instrument on satellite Polar BEAR is the first to obtain narrow band UV images for more than one band at a time. This provides the opportunity to do serious quantitative analysis of the data in terms of composition and the energy sources producing the emission (aurora and dayglow). Analysis of auroral imaging data from two passes will be presented. On one of these, simultaneous images were obtained at 1356 Å (OI 1356 Å plus N_2 LBH), 1596 Å (LBH), and 3914 Å (N_2^+ 1N). On the other, the observed bands were centered at 1304 Å (OI 1304 Å), 1544 Å (LBH), and 3914 Å. Variations in data ratios among the three bands for either pass exceeded a factor of three over the portion of the auroral oval seen within the images. The possible causes of these variations are changes in the hardness of the precipitating particle spectrum (here the particles are assumed to be electrons), changes in the abundance of O relative to N_2, changes in the albedo at 3914 Å, and statistical fluctuations where signals were low. To interpret the data, yields (Rayleighs/(erg $cm^{-2}s^{-1}$)) and yield ratios appropriate to the band centers and their widths were calculated versus hardness of the

14. SUBJECT TERMS Aurora Remote sensing Ultraviolet	Electron fluxes Electron densities Electron transport	15. NUMBER OF PAGES 72
		16. PRICE CODE

17. SECURITY CLASSIFICATION OF REPORT Unclassified	18. SECURITY CLASSIFICATION OF THIS PAGE Unclassified	19. SECURITY CLASSIFICATION OF ABSTRACT Unclassified	20. LIMITATION OF ABSTRACT SAR

precipitating electron spectrum. The calculations used MSIS model atmospheres with O density scalings of 1.0 and 0.5. The input parameters were appropriate to the times at which the data were collected and to the regions observed. Incident electron spectra were characterized by modified Gaussian and Maxwellian energy distributions defined in terms of characteristic energy E_0 (in keV) and energy flux Q (in ergs $cm^{-2}s^{-1}$). Modifications included the addition of low energy tails (for both types of distributions) and high energy tails (for Gaussians). Results are in the form of profiles of Q and E_0 versus latitude for selected cuts through the images at three different swath widths. Maximum Q values exceed 20 ergs $cm^{-2}s^{-1}$ which correspond to significant energy deposition. Derived E_0 values commonly correlate with Q and have magnitudes consistent with satellite particle data over the past several years. E_0 profiles are shown for the above O scalings and for two different 3914 Å albedo factors to demonstrate sensitivity to these parameters. Comparisons of E_0 profiles from different data ratios suggest a latitudinal variation in O with a depletion where maximum energy deposition occurred.

Accesion For		
NTIS CRA&I		✓
DTIC TAB		☐
Unannounced		☐
Justification		
By		
Distribution /		
Availability Codes		
Dist	Avail and / or Special	
A-1		

ED 2

TABLE OF CONTENTS

FIGURES

TABLES

PLATES

Plate 1

Plate 2

1. INTRODUCTION

This report covers three years of activity under Phillips Laboratory Contract No. F19628-88-C-0113. The items addressed are listed in the next paragraph. Most of our effort was directed to modeling of auroral electron transport and associated optical emissions as well as data analysis (AIRS optical data, J/Sensor particle data (see item 5 below), and Sondrestrom incoherent scatter radar data (see item 4 below)). This report discusses our efforts to determine spectral characteristics of precipitating electrons from AIRS UV images obtained at high northern latitudes on January 12 and 29, 1987.

Extensive documentation has been provided through the reports preceding this final report. The topics which have been addressed are the following:

1. Modeling of auroral UV emissions for a variety of incident electron spectra. This is in the form of yields (Rayleighs/(erg $cm^{-2}s^{-1}$)) for OI 1356 Å, OI 1304 Å, N_2 LBH bands, and N_2^+ 3914 Å.

2. Application of these yields to analysis of UV data obtained by the AIRS instrument on satellite Polar BEAR. Our efforts were directed to determining spectral characteristics of precipitating electrons (energy flux Q in ergs $cm^{-2}s^{-1}$ and characteristic energy E_o of the assumed distribution in keV).

3. Detailed statistical study of AIRS data leading to error bars on the data and on inferred values of Q and E_o.

4. Inferring incident electron spectra and corresponding intensities of the above features (excluding OI 1304 Å) from electron density profiles obtained with the Sondrestrom incoherent scatter radar. This was done to compare the radar inferred emission rates with those from the coincident AIRS data (see Robinson et al., 1991).

5. Calculation of intensities of the above features (excluding OI 1304 Å) using incident electron spectra obtained by the J/sensor on satellite HILAT (D. Hardy, private communication). These intensities were compared with AIRS data for near coincident observing situations.

6. Investigation of a new approach to solving the Boltzmann equation for auroral electron fluxes. The motivation was to provide a solution in less time than that obtained from the current CPI model. Efforts under the current contract were limited to defining the approach.

7. Initiation of a software project to provide Phillips Laboratory with thermospheric UV codes for incorporation into AURIC (Atmospheric Ultraviolet Radiance Integrated Code).

Related to some of the above activities was a restructuring of the user-friendly front end of our auroral model. A screen editing version now exists which makes it relatively easy to input the parameters needed for multiple runs of the full auroral model.

We will not discuss all of the above topics in this report. Specifically, topics 4 - 7 along with the just discussed code restructuring will be omitted. Our findings were inconclusive concerning topics 4 and 5. One of our goals was to test the AIRS inferred Q and E_o values against those based on the radar and J/sensor data. In the case of the J/sensor, there was a 10 minute separation between its measurements and those of AIRS which was the minimum time separation that could be achieved for the available data sets. Changes occurred in the auroral precipitation along the HILAT track over these ten minutes. In the case of the radar data, we did find reasonable agreement between the radar inferred UV emission rates and the AIRS measurements. Given the poor counting statistics, we did not compare the Qs and E_os between the two data sets. We refer the reader to a paper recently written by Robinson et al. (1991) for more detailed information on this topic. Topic 7 has been documented in Quarterly reports 10 - 12. Most of our AURIC software development is expected to occur in a subsequent contract.

2. EXPERIMENT AND PASSES OF INTEREST

The Polar BEAR satellite, carrying the AIRS auroral imager experiment, was launched from Vandenberg AFB on 13 November 1986 and placed in a near-circular polar orbit with an altitude of approximately 1000 km (1012 km apogee, 970 km perigee) and an inclination of 89.55°. Figure 1 provides a vertical perspective projection showing the Polar BEAR orbit at a time when it is visible to ground stations to be discussed below. The shaded region depicts the global coverage obtained by the AIRS imager. The boundaries of a statistical auroral oval are included in the projection to illustrate the coverage of the auroral zone by AIRS. The Polar BEAR satellite was named for its polar orbit and for its mission: Beacon Experiment and Auroral Research. The experiment name AIRS is an acronym for Auroral and Ionospheric Remote Sensor.

The AIRS sensor could operate as an imager, spectrometer, or photometer. In imager mode, a rotatable mirror (called the scanning mirror) at the entrance aperture moved the field-of-view in the cross track direction. The line-of-sight extended 5.4° above the hard earth on each side giving a field-of-regard of 130.4°. In the spectrometer and photometer modes, AIRS viewed only in the nadir direction.

In the imaging mode, 326 pixels compose a single line scan (over the 130.4° field-of-regard) with an integration period of 6.83 milliseconds/pixel. Data were collected simultaneously in four wavelength channels (two far ultraviolet (FUV) wavelengths, 3914 Å and 6300 Å; data at the latter wavelength will not be discussed in this report). As the satellite proceeded along its track, the cross track scan was repeated every three seconds. Since the satellite had no recorder, data were only acquired when Polar BEAR was in contact with ground receiving stations. The primary permanent receiving stations were at Sondre Stromfjord, Greenland, and at Tromso, Norway, which limited most observations to high latitudes and limited data acquisition time per image to about 10 minutes.

The instrument is similar to the previous imager flown by the Geophysics Directorate,

Fig. 1 Vertical perspective projection showing Polar BEAR orbit and area viewed by AIRS

Phillips Laboratory (previously Air Force Geophysics Laboratory) on the HILAT satellite in 1983 (Schenkel et al., 1985). Although the design differs in some aspects, the line scan mirror, the telescope, and the use of a spectrometer as a tunable FUV 'filter' remain the same. Atmospheric radiation entering the telescope from the scanning mirror is focussed on the entrance slit of the spectrometer, which has two exit slits and separate photomultipliers, providing for two FUV channels separated by 240 Å. The pairs of channels of interest here are [1304 Å, 1544 Å] and [1356 Å, 1596 Å]. The FWHM (full width half maximum) spectral resolution is 36 Å which is sufficient to separate the bright 1304 Å feature from 1356 Å.

Images at the third wavelength of interest here, namely at 3914 Å, (N_2^+ 1N (0,0)), are obtained by light passing through a hole in the telescope mirror onto a 3914 Å interference filter with a 10 Å FWHM bandpass. Thus, the 3914 Å image is spatially coincident with the FUV images although at a somewhat different spatial resolution to be discussed below.

Figure 2 shows the features observed by AIRS for a resolution of 36 Å centered on 1356 Å, 1544 Å, and 1596 Å. A panel is not included for the 1304 Å channel since the only important feature in this channel is OI 1304 Å. The triangles provide an idealistic representation of the instrument response function for 36 Å resolution. The dotted curves are synthetic spectra of nadir viewing emission for an incident electron spectrum characterized by a Maxwellian distribution having a mean energy of 2 keV. Emission is composed of N_2 LBH bands and OI 1356 Å. The solid curves are convolutions of the triangles with the spectra and show that several bands contribute to the LBH signals at 1544 Å and 1596 Å. At 1356 Å, LBH 1354 Å is blended with OI 1356 Å and varies in its relative importance as the hardness of the incident electron spectrum changes (to be further discussed in Section 4).

The field-of-view (FOV) of the FUV images is 0.373° in the slit width direction, which is also cross-track with respect to the satellite orbit. The along-track direction, which is also the slit length direction, has a FOV of 1.53°. For the assumed emission altitude of 110 km, the nominal spatial resolution per pixel is about 5 km cross-track and 20 km along-track. For the 391.4 channel, the FOV is slightly larger: 1.49° cross-track and 2.25° along track. A more de-
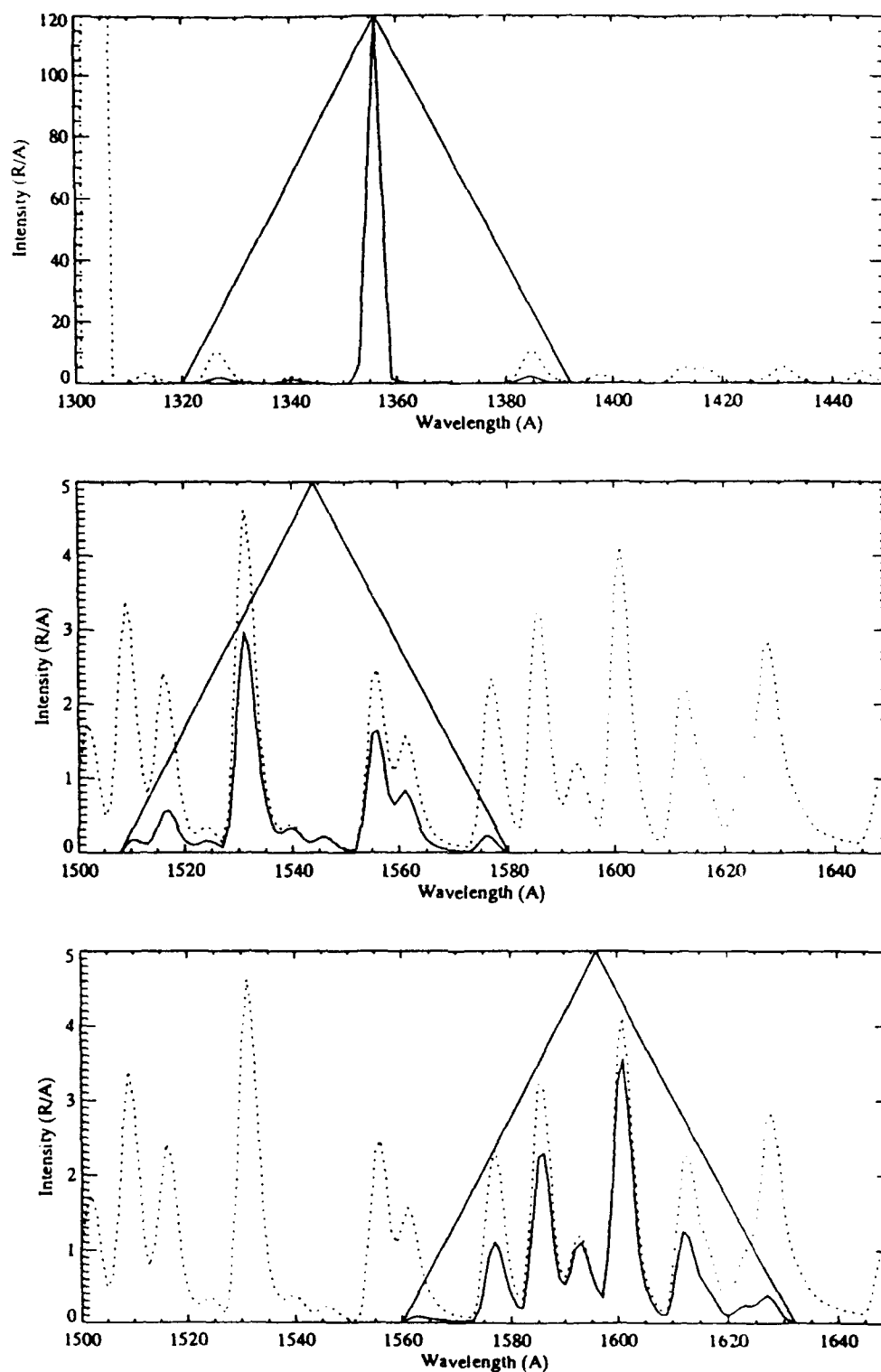
Fig. 2 Nadir viewing synthetic spectra showing emission features within the FUV spectrometer bandpasses centered at 1356 Å, 1544 Å, and 1596 Å. Also shown are idealized instrument response functions for 36 Å resolution and convolutions of these functions with the spectra

tailed discussion of the instrument is given in Schenkel et al. (1986).   AIRS was calibrated and tested in the Ultraviolet Calibration Facility at the Geophysics Directorate, Phillips Laboratory, Hanscom AFB, Massachusetts. The AIRS sensor was calibrated against secondary detector standards supplied by the National Institute for Standards and Technology (NIST), using a calibration facility and techniques developed for previous space experiments. A collimated beam of known brightness irradiates the sensor and the number of counts is recorded to establish the sensitivity. The sensitivities for use with the passes analyzed in this paper are given in Table 1.

Table 1. Calibration Factors for Wavelengths of Interest

Wavelength	Calibration Factor (Rayleighs/counts/s)
1304 Å	50.0
1356 Å	57.8
1544 Å	168.0
1596 Å	208.0
3914 Å	328.9

The data analyzed here are from single passes on January 12 and January 29, 1987. Plates 1 and 2 show the 1356 Å and 1304 Å images from these passes and north/south cuts marking the regions investigated in this work. The two FUV channels on the Jan 29 pass were 1356 Å and 1596 Å. The FUV channels on the Jan 12 pass were 1304 Å and 1544 Å. The emissions observed on January 29 were among the brightest recorded by AIRS that winter. The geomagnetic conditions throughout January of 1987 were extremely quiet, but January 29 was one of the most active days of the month. Shown in Figure 3 is the three hour a_p index at the time of both observations.
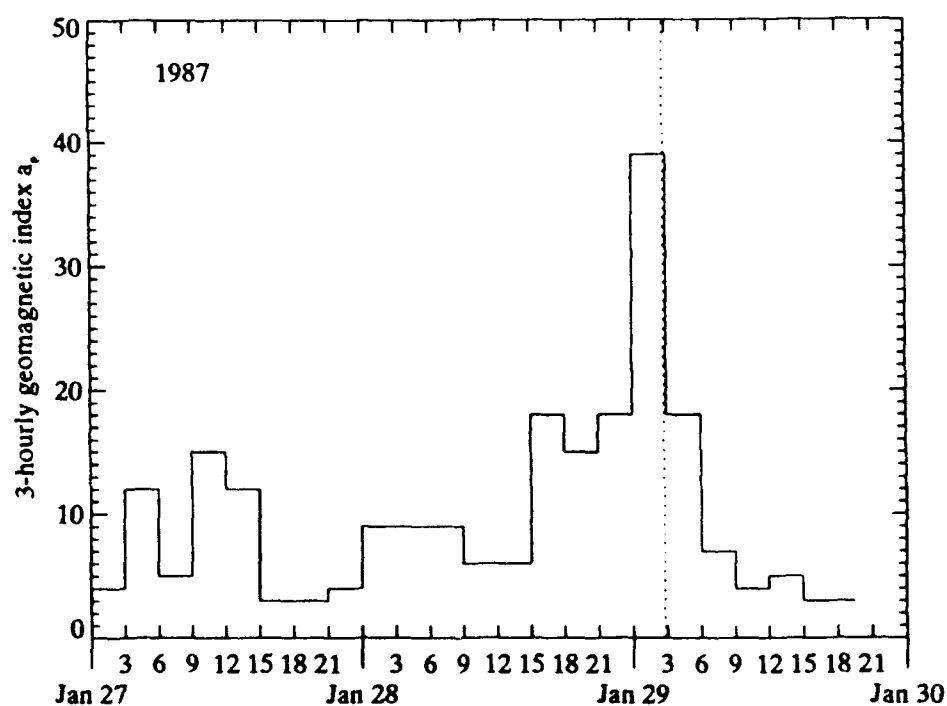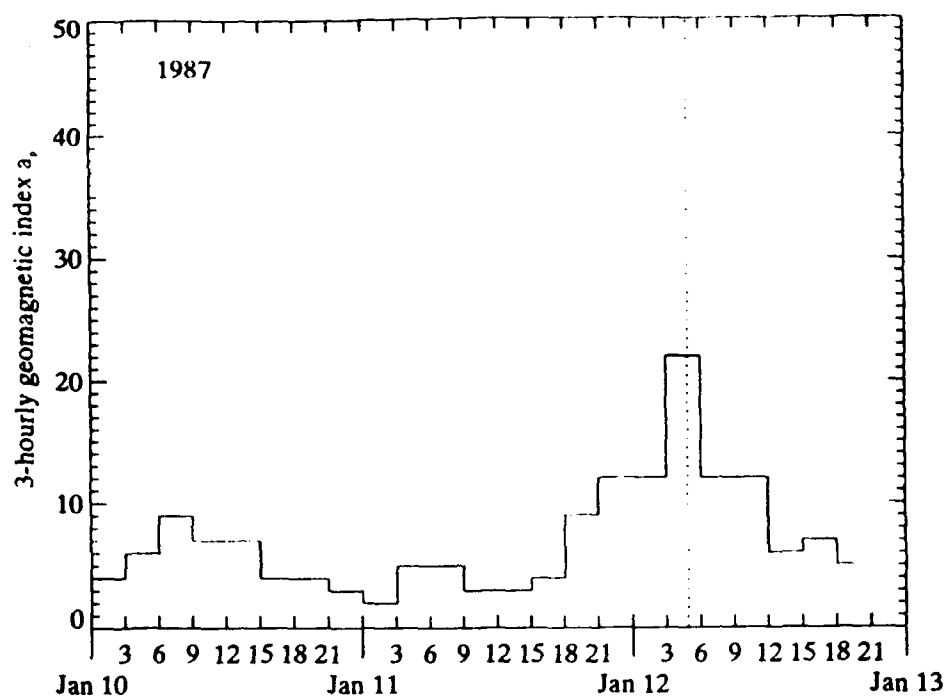
Fig. 3 The geomagnetic 3 hour index a_p over three day periods within which the observations of interest were recorded. The times of these observations are given by the vertical dotted lines

3. OVERVIEW

The key to a quantitative interpretation of AIRS auroral data is changes in emission ratios as the characteristic energy of the precipitating particle spectrum changes. With increasing hardness, energy deposition moves lower into the atmosphere where there is relatively less atomic oxygen (O) and greater attenuation at FUV wavelengths caused by pure absorption of the radiation by molecular oxygen (O_2). The observed intensities of OI 1304 Å and OI 1356 Å decrease as a result of both effects. The N_2 LBH band emissions increase due to relative increases in the N_2 density but above approximately 1 keV the observed emissions decrease with increasing energy, due to pure absorption by O_2.

3.1   Brief description of approach

Our approach is to first infer spectral hardness of the precipitating electrons from the observed intensity ratios for features such as N_2 LBH 1596 Å and N_2^+ 1N 3914 Å. This is done using calculated ratios as functions of spectral hardness, composition, and albedo (applies to 3914 Å). The energy flux associated with this spectral hardness is then obtained from the absolute intensity of 3914 Å after accounting for albedo. This is done along vertical cuts (north/south) through the images. Data are summed over several pixels in the east/west direction to improve statistics. Spectral hardness and energy flux are then displayed versus latitude for a given cut.

3.2   Characterizations of incident electron spectra

We assume that only electron precipitation is important for producing the recorded emission. Portions of the image may contain important contributions from proton/H atom precipitation. We have no way of knowing this, however, since HI Lyα was not recorded. Statistically, proton/H atom precipitation is a minor source of energy deposition across the nightside of the auroral oval (of interest to this work) and will not affect our conclusions (Hardy et al., 1989).

The energy vs. number flux of most electron precipitation can be characterized by modified Maxwellian (diffuse aurora) and modified Gaussian (discrete aurora) distributions. More will be said about this below. Modifications refer to the presence of high and low energy tails. Calculated intensities and their ratios will be presented in the next section versus E_o for each type of distribution with Q set to 1 erg $cm^{-2}s^{-1}$. For Maxwellian distributions, E_o gives the energy of its peak (broad maximum) and is half of its mean energy in the absence of tails. For Gaussian distributions, E_o also refers to the energy of its peak (often referred to as the "monoenergetic" peak in particle data papers) and is close to its average energy in the absence of tails. A description of the two distributions with tails is given in Strickland et al. (1991) (also see Meier et al., 1989 for more details on the low energy tail added to the Maxwellian distribution).

3.3   Interpretation of results

The result that would most directly relate to the data is an altitude profile of energy deposition. This distribution determines the ratio of intensities for a given set of neutral density profiles and albedo at 3914 Å if this feature is involved. It should first be made clear that a unique deposition profile cannot be obtained from nadir observations. The shape of the incident electron spectrum must be assumed in order to interpret a given data ratio. Applying this shape, we obtain E_o and Q from the data which can then be related to either an energy deposition profile or volume emission rates of the features of interest. Different profiles result from assuming a modified Gaussian distribution compared to, say, a modified Maxwellian distribution. Hopefully, useful deposition information is obtained regardless of the parameterized form of the incident electron spectrum. If so, it can be used to calculate electron density profiles (EDPs) and associated conductivities. To examine this issue, the inferred E layer parameters $h_{max}E$ (altitude of maximum electron density in the E region) and $N_{max}E$ (density at $h_{max}E$) will be presented in addition of E_o and Q. These will come from time dependent calculations of the EDP using the inferred E_o and Q values for modified Maxwellian and Gaussian distributions.

3.4   Connection with other data

We will attempt to relate our results to particle data and theory on electron precipitation in the premidnight auroral oval. This is especially important since we have no independent coincident data, such as from a ground based radar or on-board particle detector, to verify our results. Comparing with published particle data is difficult since much of the attention in many published articles has been directed to details in the shape of precipitating electron spectra. Details which are not important to optical emissions. For example, there is considerable interest in the properties of the spectrum below a keV (referred to above as a low energy tail). This portion of the spectrum has an important impact on mean energy but little impact on absolute optical intensities or their ratios for the emissions of interest here. Therefore, we will not compare mean energies, such as those of Hardy et al. (1985), with those obtained from our inferred spectra.

Discrete auroral spectra

A large body of literature exists on auroral electron spectra. Extensive measurements have been made from low and high altitude satellites (e.g., DE-1, DE-2, AE-C, AE-D, ISIS-1, ISIS-2, NOAA-6, S3-2, S3-3, DMSP, P78-1, and HILAT) and from rockets (e.g., Arnoldy et al., 1974, McFadden et al., 1990, and references therein). Much of the attention has been directed to spectra exhibiting "monoenergetic" peaks and field alignment of the precipitation. These spectra are associated with discrete auroras and often with inverted-V events (Frank and Ackerson, 1971 and e.g., Lin and Hoffman, 1982). It is believed that such spectra in the auroral zone arise from acceleration of plasma originating in the central plasma sheet and plasma sheet boundary layer of the magnetosphere. Acceleration through a field-aligned electrostatic potential above the ionosphere will produce spectra exhibiting a "monoenergetic" peak (see recent review by Burch, 1991 and earlier papers such as Knight, 1973, Evans, 1974, Chui and Schulz, 1978, and Lyons, 1981). Acceleration via wave particle interactions has been suggested for producing field-aligned precipitation over broad energy ranges. Such spectra are observed in precipitation events commonly called bursts (e.g., Temerin et al., 1986 and McFadden et al., 1987). Bryant

(1987), Bryant et al. (1991) and Bingham et al. (1988) provide examples of theoretical work suggesting larger roles for wave particle interactions than just for producing burst-type precipitation.

Diffuse auroral spectra

Less attention has been directed to the broader, more isotropic spectra which do not require acceleration mechanisms. These typically exhibit a Maxwellian shape with the presence of a low energy tail (see, e.g., Sharber, 1981 and Schumaker et al., 1989). Such spectra are believed to arise from plasma sheet electrons injected into the loss cone by pitch angle diffusion. The diffuse aurora, important in its overall energy content, is produced by this type of precipitation and when fit to a Maxwellian distribution, E_o is typically around 1 keV.

Expected range of spectral hardness based on particle data

An appropriate measure of the hardness of precipitating electron spectra for either diffuse or discrete auroras is the altitude region of maximum energy deposition. This will also be the altitude of maximum electron density. As noted above, we prefer to test our inferred spectra against expectations based on particle data by using a parameter such as $h_{max}E$ since it is not sensitive to details in the shape of the spectrum. Figure 4 gives $h_{max}E$ versus E_o for modified Maxwellian and Gaussian distributions. We note that similar values occur at E_o and $2E_o$ respectively for Maxwellian and Gaussian distributions. This relationship produces approximately the same mean energy (excluding low energy tails) which in turn leads to similar altitude regions of maximum energy deposition.

Different h_{max} values, however, are obtained from the optical data assuming these two distributions. In fact, it will be shown that h_{max} based on a modified Maxwellian spectrum is somewhat larger due to the broader altitude distribution of energy deposition. Furthermore, E_o based on a Maxwellian distribution is closer of 1/3 than 1/2 of the Gaussian based E_o. We will
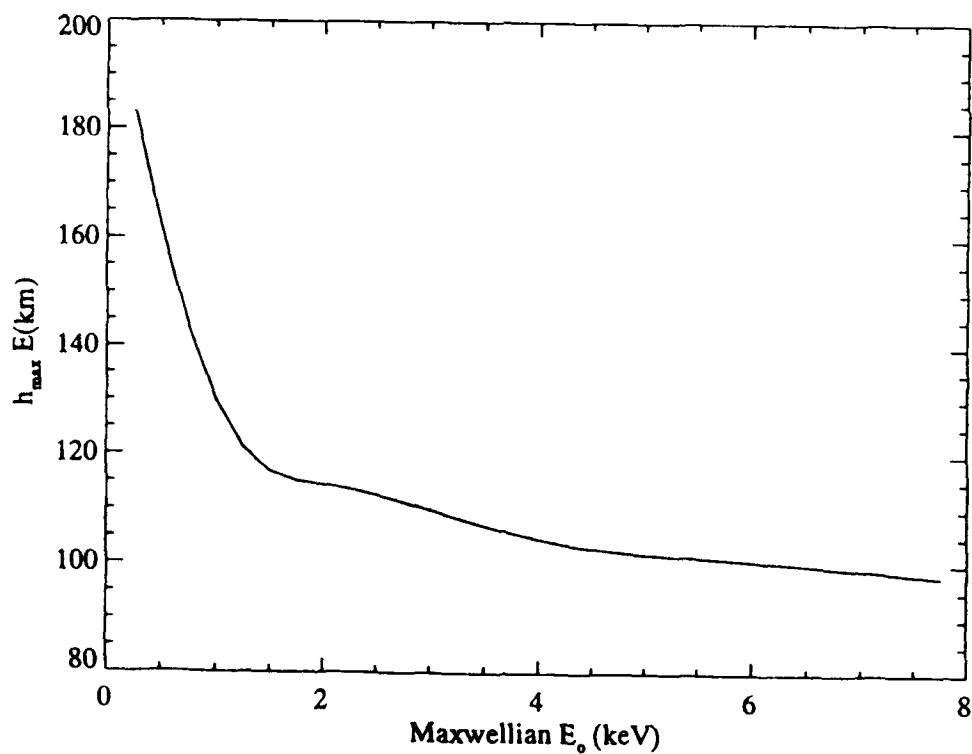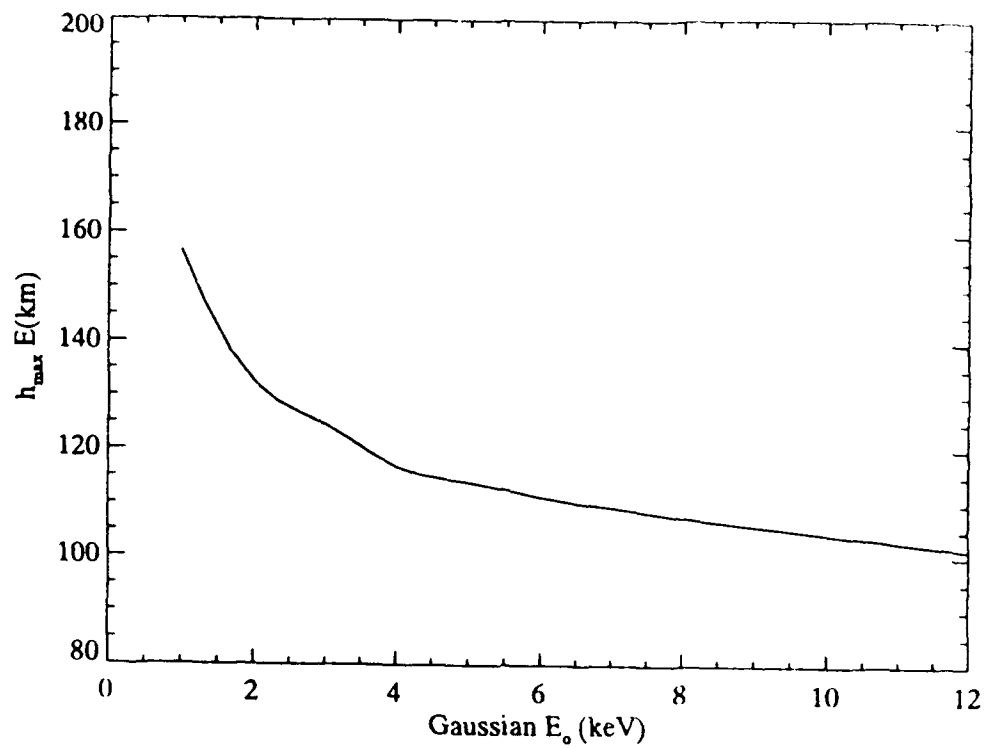
Fig. 4 Altitude of maximum electron density in E region, $h_{max}E$ versus E_0 for modified Gaussian (upper panel) and Maxwellian (lower panel) distributions

show in Section 7, for example, that for an inferred value of E_o = 8 keV based on a Gaussian distribution, that the corresponding Maxwellian E_o is about 3 keV. This shows that the altitude distribution of energy deposition changes intensity ratios in addition to mean energy. The differences in energy deposition versus altitude for Maxwellian and Gaussian spectra inferred from the same optical data is shown in Figure 5 in the form of electron density profiles for the example just cited (Gaussian E_o = 8 keV and Maxwellian E_o = 3 keV). As expected, the peak obtained from the Gaussian distribution is sharper and occurs lower in the atmosphere. This figure illustrates the degree of uncertainty to be expected in inferred conductivities or electron density profiles when lacking information about the shape of the incident electron spectrum.

Data were obtained from bright active aurora. If we assume much of this is discrete aurora, E_o values (for modified Gaussians) from a few keV to > 10 keV are reasonable. This corresponds to $h_{max}E$ values from about 130 to 100 km. As will be shown in Sections 7 and 8, our inferred E_o and $h_{max}E$ values are within these expected ranges.
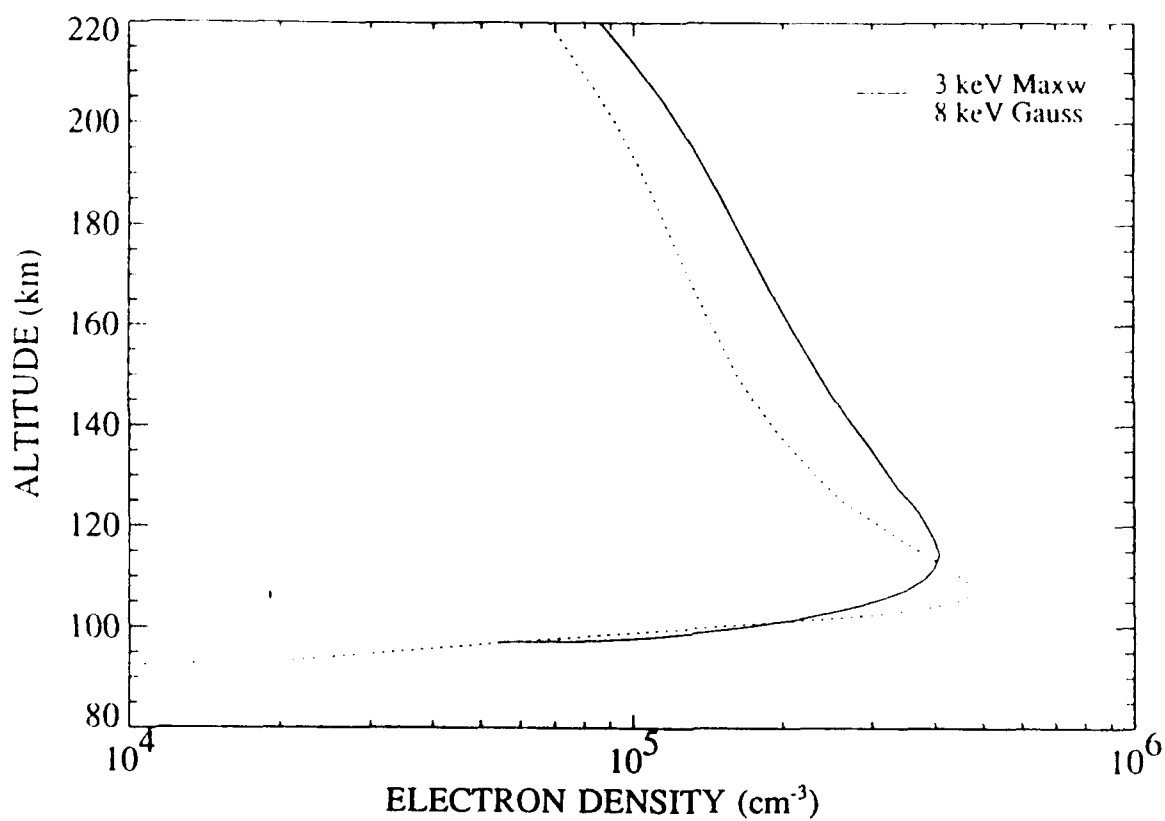
Fig. 5 Electron density profiles for modified Gaussian and Maxwellian distributions having E_o values of 8 and 3 keV, respectively

4. APPLIED MODEL

4.1 Cross sections

Figure 6 shows the electron impact cross sections used to calculate the yields. Table 2 provides references to the original values and scaling factors used in these calculations to adjust the published cross sections. The cross sections in Figure 6 contain these scaling factors.

Table 2. Emission Cross Section References and Scaling Factors

Feature		Cross Section Reference	Applied Scaling Factor	Scaling Factor Reference
OI 1304 Å	(e^-+O)	1	1.42	2
OI 1356 Å	(e^-+O)	3	0.36	1
OI 1356 Å	(e^-+O_2)	4	0.29	5
N_2 LBH	(e^-+N_2)	6	0.88	7
N_2^+ 1N 3914 Å	(e^-+N_2)	8	0.65	9

1. Zipf & Erdman (1985)
2. Meier (1991)
3. Stone & Zipf (1974)
4. Wells et al. (1971)
5. R. Link (private communication, 1992) based on Ajello (1971) and Erdman and Zipf (1987)
6. Ajello & Shemansky (1985)
7. Emission part of excitation cross section (Ajello and Shemansky (1985)
8. Borst & Zipf (1970)
9. Fraction of emission of the first negative system within this band (Vallance Jones, 1974)

4.2 Model atmosphere

MSIS86 (Hedin, 1987) was used to generate the model atmospheres for our analysis of data from the two passes identified in Section 2. The MSIS86 parameter values used for each
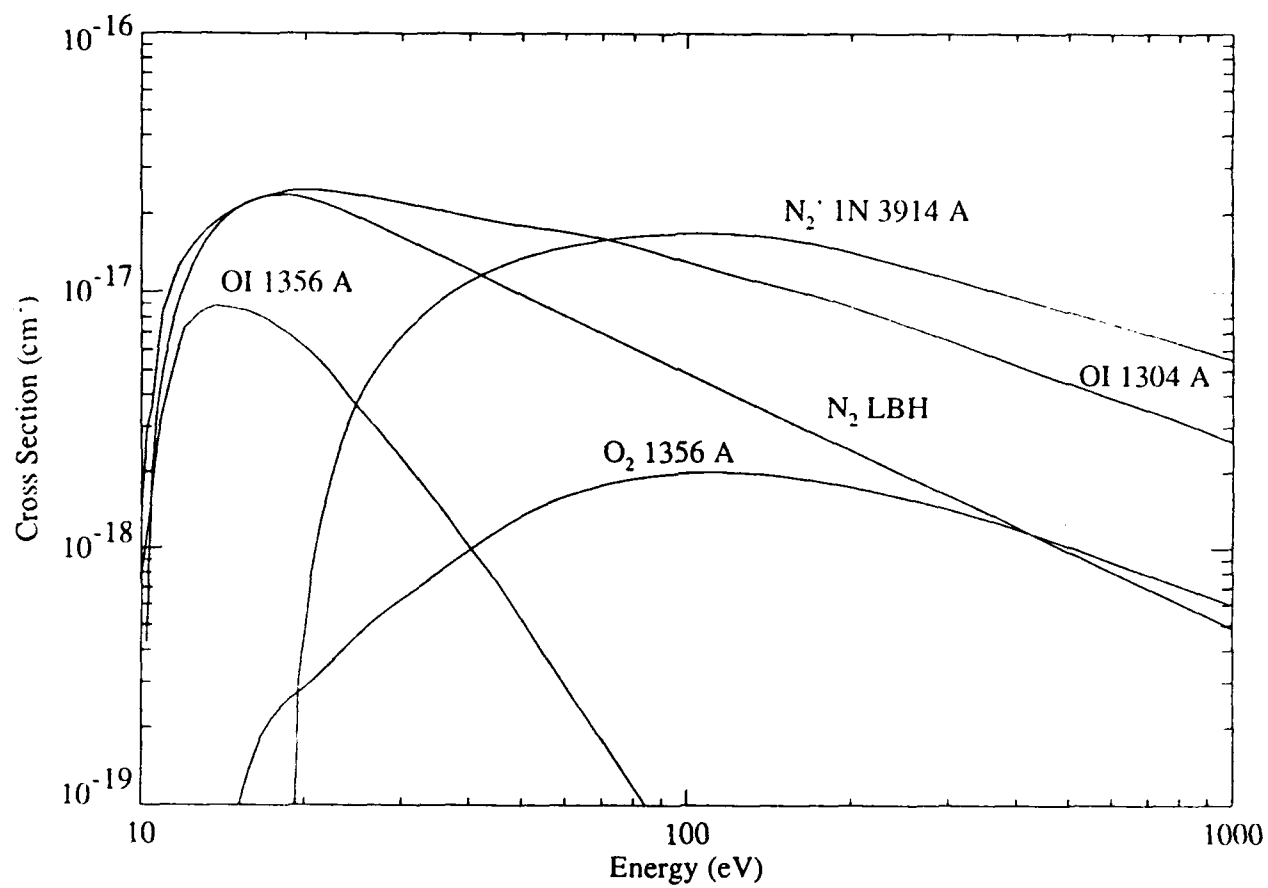
Fig. 6 Applied emission cross sections

day are given in Table 3. The same conclusions would have been drawn had only a single atmosphere been used for both passes given the similarity between the atmospheres and the uncertainties associated with the calculated yields and data. For these reasons, we will show yields for only the Jan 29 pass in Section 4.4.

Table 3. MSIS86 Parameter Values

Parameter	Jan 29 Pass	Jan 12 Pass
Year	1987	1987
Day	29	12
UT (sec)	10548	17892
Latitude	57° N	60° N
Longitude	59° W	75° W
F10.7	70.8	68.0
<F10.7>	72.0	72.0
A_p	10	10

4.3 Incident electron spectra

As noted in Section 3, both Gaussian and Maxwellian energy distributions were used to calculate the emission yields. A Gaussian distribution is more typical for discrete aurora while Maxwellian is typical for diffuse aurora. On a global scale both will be observed. On a pixel scale size, AIRS data alone are not sufficient to determine whether the precipitating energy spectrum producing the emission is more Gaussian or Maxwellian. Some indication will come from the structure in surrounding pixels and from the intensity. For example, if a pixel is within a bright part of the image associated with many ergs $cm^{-2}s^{-1}$ of precipitation, the aurora here is unlikely to be diffuse and will generally be better characterized by a Gaussian distribution. We have not attempted to selectively apply a given distribution based on the morphological content with the images. Instead, both distributions have been used to infer E_0 and Q followed by

comparisons between the two representations. Most of the results presented, however, are based on Gaussian distributions since they are more appropriate for the selected data which, on the average, correspond to several ergs $cm^{-2}s^{-1}$ of precipitation.

A description of the distributions used is given by Strickland et al. (1991). Low energy tails have been added to both types of distributions, and a high energy tail has been added to the Gaussian distribution. Figure 7 shows families of these distributions for $Q = 1$ erg $cm^{-2}s^{-1}$.

4.4 Emission yields

We use the model of Strickland et al. (1976) (further described by Strickland et al., 1983, Strickland et al., 1989, Meier et al., 1989, and Strickland et al., 1991) to calculate transport and energy degradation of the incident electrons and all secondaries produced during the degradation process. The solution is in the form of the electron flux $\phi(z,E,\mu)$ $(e^-cm^{-2}s^{-1}eV^{-1}sr^{-1})$ as a function of altitude z, energy E, and cosine of the pitch angle μ. Typical grids in these variables include about 30 altitudes, 40 energies, and 20 angles.

The needed volume excitation rates j(z) are obtained from the integral

$$j(z) = n(z) \int \sigma(E)\phi(z,E,\mu)2\pi d\mu dE \qquad\qquad cm^{-3}s^{-1} \qquad (1)$$

where n(z) is the density (cm^{-3}) of the species involved in electron impact excitation of the emitting state and σ is the electron impact cross section (cm^2). The excitation rate equals the observed emission rate for the LBH and 1N bands. The excitation rate is less than the emission rate for 1304 Å and 1356 Å due to multiple scattering. We designate the emission rate in this situation as S(z) which we have calculated from the equation of radiative transfer using the model of Strickland and Anderson (see, e.g., Strickland and Anderson, 1983).
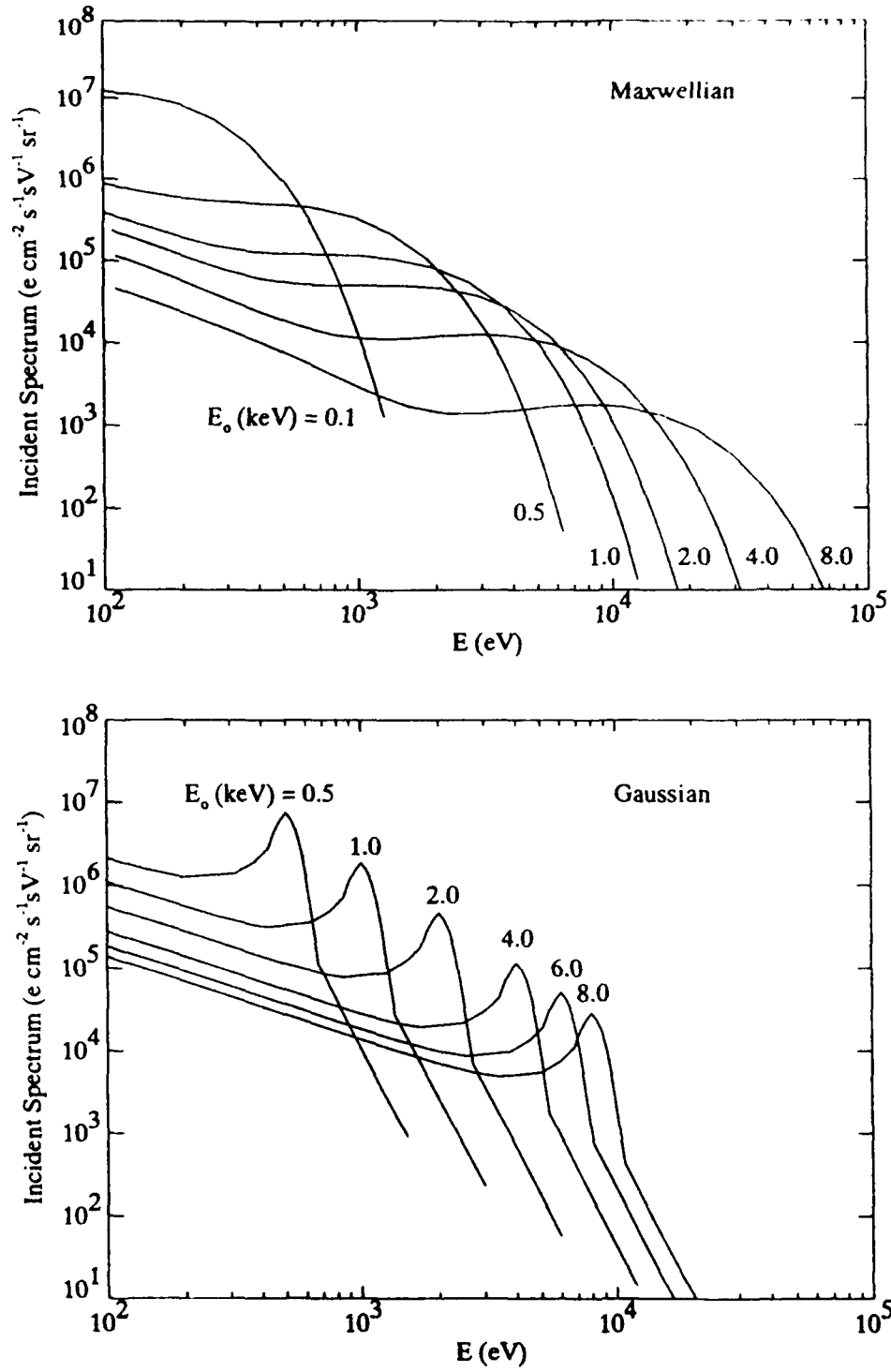
Fig. 7 Examples of modified Maxwellian (upper panel) and Gaussian (lower panel) distributions used to characterize the incident electron spectrum. The energy flux $Q = 1$ erg $cm^{-2}s^{-1}$ for all spectra

The column emission rate $4\pi I$ for 3914 Å is

$$4\pi I = 10^{-6} \int j(z)dz \qquad \text{Rayleighs} \qquad (2)$$

For any given LBH band, this generalizes to

$$4\pi I = 10^{-6} \int j(z)e^{-t(z)}dz \qquad (3)$$

where $t(z)$ is the optical depth for pure absorption by O_2 at the wavelength of the band. For 1304 Å and 1356 Å, the equation further generalizes to

$$4\pi I = 10^{-6} \int S(z)T(z)e^{-t(z)}dz \qquad (4)$$

where $T(z)$ is the transmission function for self absorption. The intensity for each of the above formulas is related to its corresponding emission yield by

$$4\pi I = QY \qquad (5)$$

where yield Y is the column emission rate for $Q = 1$ (1 erg $cm^{-2}s^{-1}$). This displays the expected linear relationship between emission brightness and incident energy flux.

Figure 8 shows examples of calculated nadir viewing column emission rates when viewing from above the emission layer. These spectra are for incident electron spectra characterized by Gaussians for $Q = 1$ erg $cm^{-2}s^{-1}$ and $E_0 = 2$ and 10 keV. The spectra are comprised of LBH bands, OI 1304 Å, OI 1356 Å, NI 1493 Å, and NI 1743 Å.

The LBH spectra in Figure 8 are based on calculated column emission rates and on an O_2 pure absorption cross section peaking at 1.5×10^{-17} cm^2. At a given wavelength, the total column emission rate was obtained by interpolation knowing the cross section at this wavelength. The synthetic spectral routine used was developed by R. Conway (private communication, 1990) and it provides a line by line description based on a given rotational temperature. The LBH emissions in Figure 8 were obtained on a 1 Å grid with smoothing to give a resolution of 20 Å. The atomic lines were added with appropriate smoothing.

Figures 9 and 10 shows yield (Y) versus E_0 for Gaussian and Maxwellian distributions. The Jan 29 pass MSIS model atmosphere (see Table 3) was used to generate these yields. One set was obtained with no scalings (solid curves) and a second was obtained with the O density scaled by .5 (dotted curves). The second set of results show the dependence on O density which is believed to decreases in response to auroral heating of the lower thermosphere.

The yields of interest for analysis of the Jan 29 pass data are those of OI 1356 Å, N$_2$ LBH 1596 Å, and N$_2^+$ 3914 Å. The yields for 1304 Å and LBH 1544 Å are included since essentially these same values will be applied to analysis to data from the Jan 12 pass. The variations with E_0 have been explained in the papers by Strickland et al. (1983, 1991). The increase in the O yields with decreasing E_0 is due to a combination of decreasing O_2 pure absorption and increasing relative O abundance in the deposition region. This increasing abundance change causes the opposite behavior in the LBH and 3914 Å yields. LBH, nevertheless, rises until less than 1 keV due by decreasing O_2 pure absorption. The various FUV yields become parallel to one another at the larger E_0 values regardless of whether emission is from O or N$_2$. This is caused by pure absorption which leads to detectable emission from the same region regardless of E_0 beyond a certain value. This is an important effect since one cannot use features such as 1356 Å and 1596 Å to infer E_0 for hard spectra even if the O concentration were known. One of the features must exhibit significantly less pure absorption than the other. This can be realized using long wavelength LBH bands (beyond 1700 Å) which will exhibit a yield curve similar to that of 3914 Å but will not suffer from reflection as does 3914 Å. This approach can be expected to be used on future FUV spectrographic experiments such as SSUSI (Spectral Sensor Ultraviolet Spectro-
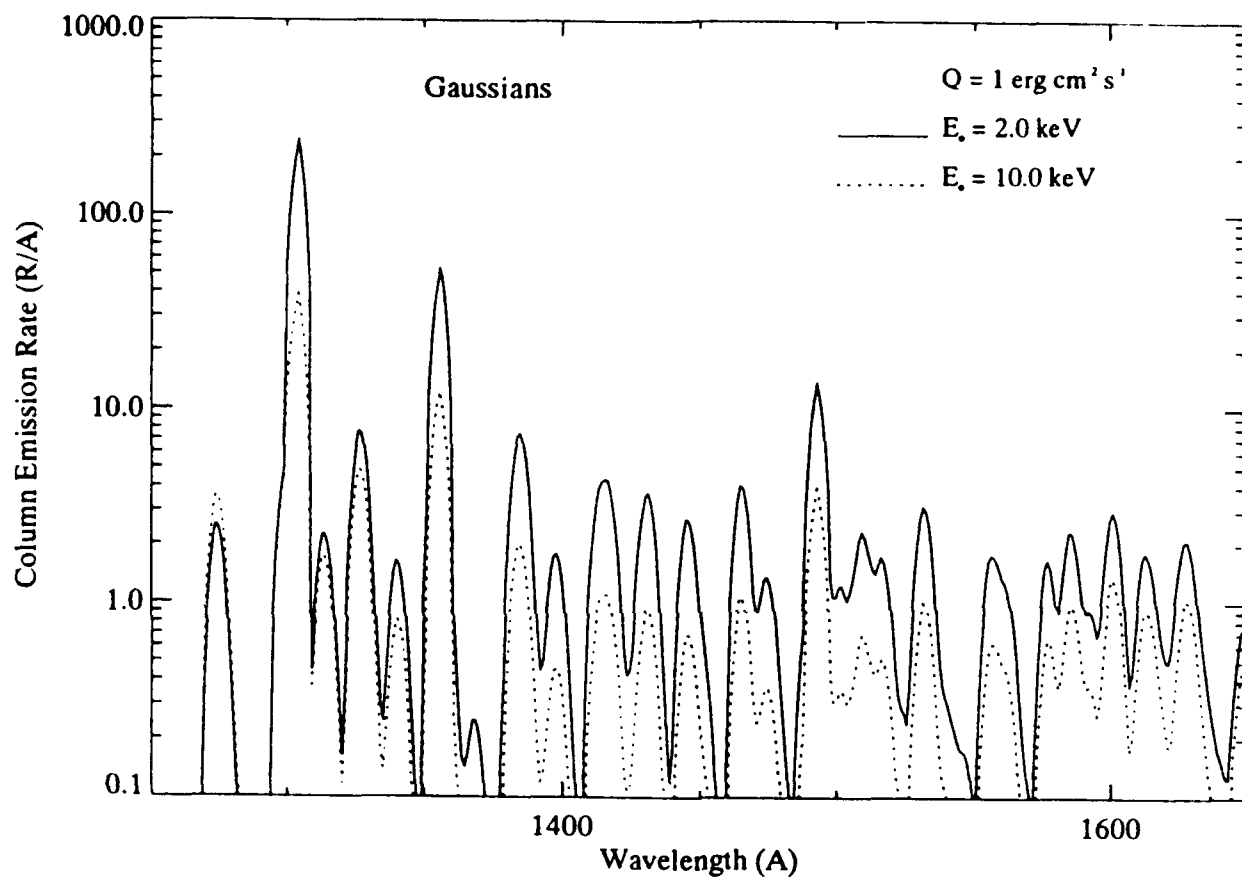
Fig. 8 Calculated nadir viewing spectra from 1250 Å to 1650 Å for incident electron spectra given by modified Gaussian distributions with E_0 values of 2 and 10 keV and Q = 1 erg $cm^{-2}s^{-1}$. The spectra include OI 1304 Å, OI 1356 Å, N_2 LBH bands, and NI 1493 Å
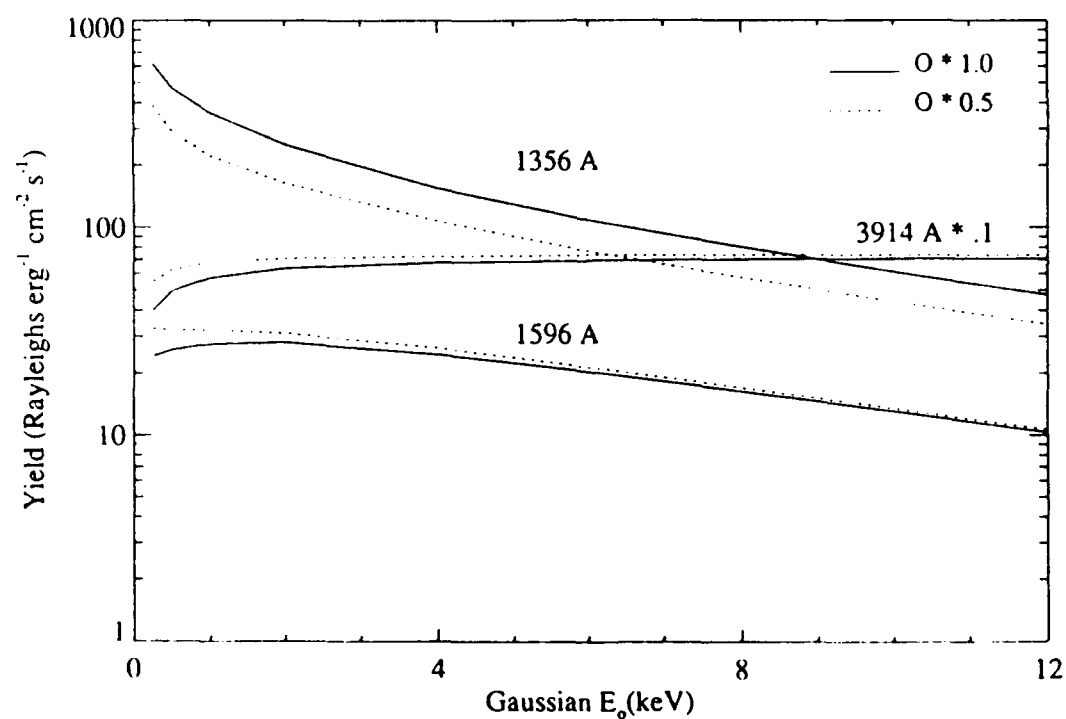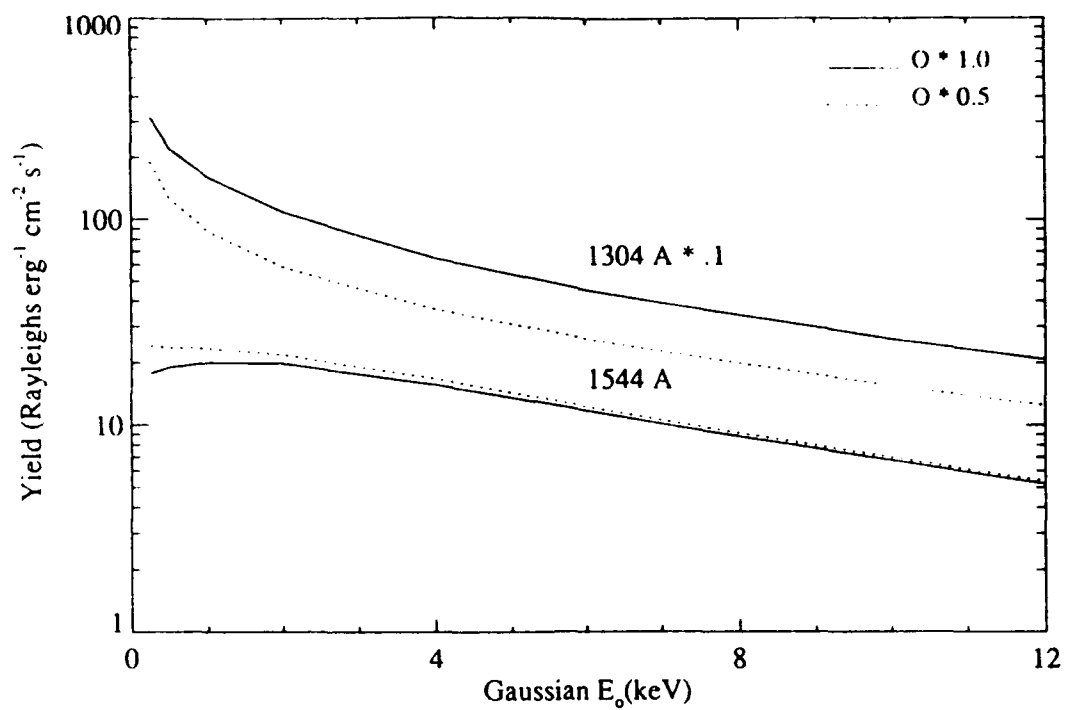
Fig. 9 Yields versus E_o for modified Gaussian distributions. The yields were obtained by convoluting an idealized instrument response function with calculated nadir viewing synthetic spectra
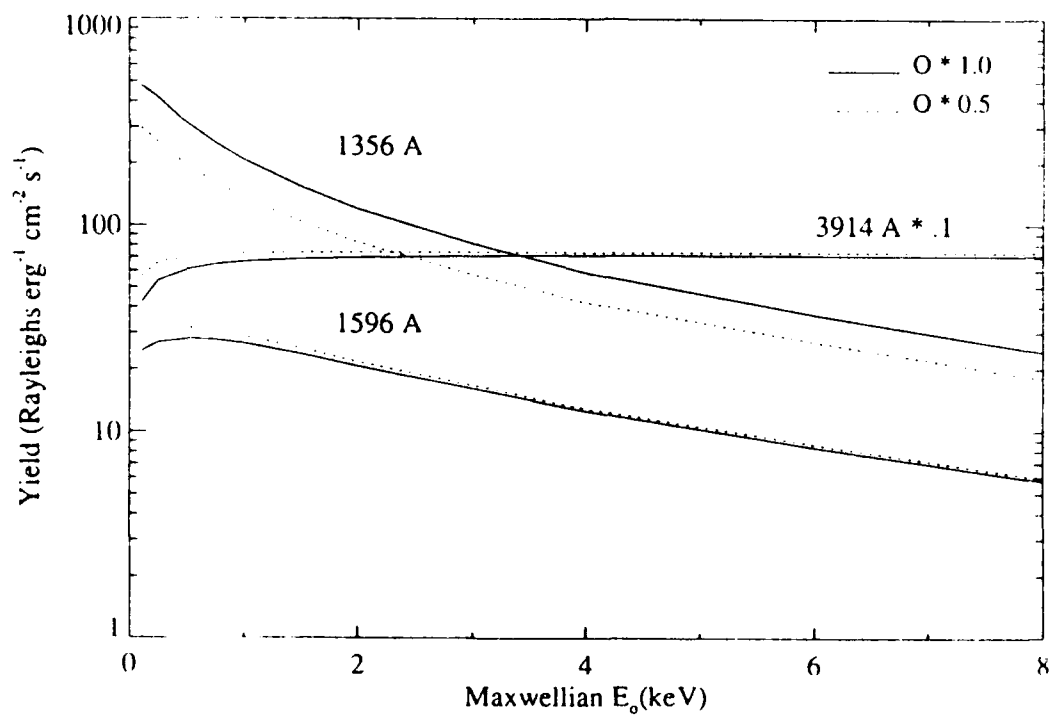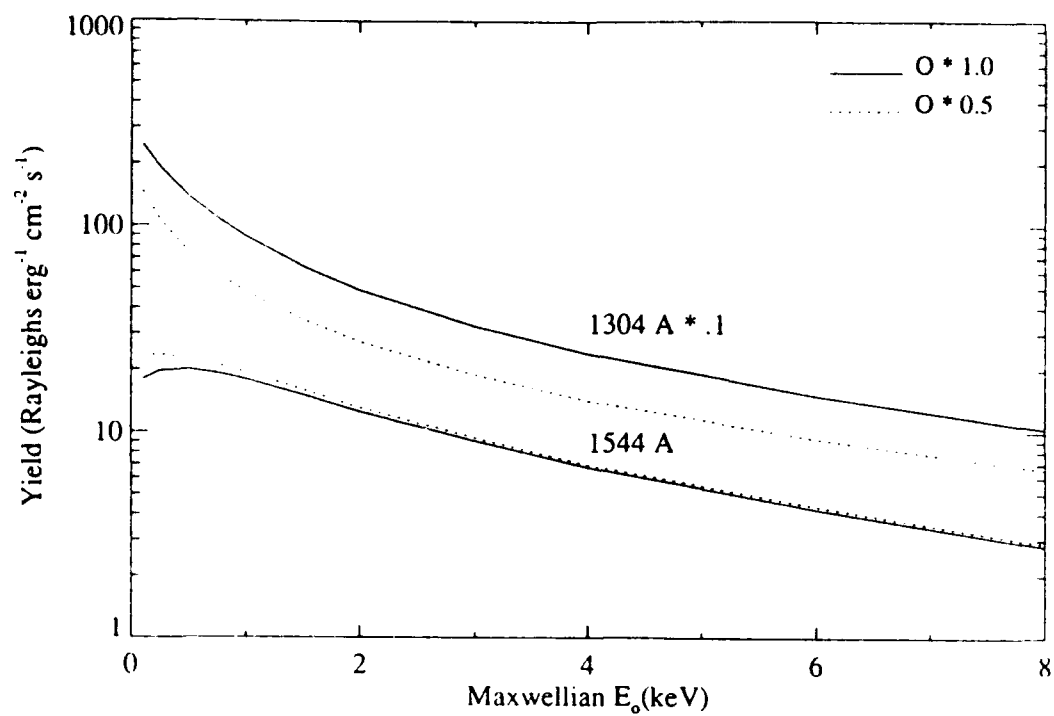
Fig. 10   Similar to Figure 9 except for modified Maxwellian distributions

graphic Imagery) on DMSP (Defense Meteorological Satellite Program) and AURA (Atmospheric Ultraviolet Radiance Analyzer).

The 1304 Å and 3914 Å yields contain only OI 1304 Å and N_2^+ 3914 Å emission. Each of the two LBH yields contains several LBH bands as was illustrated in Figure 2. The 1356 Å yield is a sum of yields for OI 1356 Å (e^- on O and e^- on O_2), and LBH (the LBH contribution is dominated by the 1354 Å band). Figure 11 displays these components along with their total for Gaussian electron spectra and for the O density profile scaled by .5. The component yields become parallel to one another above 5 keV for the reason discussed in the previous paragraph.

At 3914 Å, AIRS data contain Rayleigh scattered and reflected emission along with the direct emission by electron impact. Only the direct component is shown in Figures 9 and 10. The other components vary according to the horizontal distribution of auroral luminosity and cloud and surface conditions. Unfortunately, we do not know these latter conditions and must estimate their effect. Factors of 1.2 and 1.4 have been applied to the direct component to reflect our estimate of the range of enhancement in the AIRS data. Deduced E_0 values for these factors will be compared to one another in the next section.

Figures 12 and 13 show ratios of the yields from Figures 9 and 10. Comparisons of these with data ratios have been used to estimate E_0 values (taking into account the enhancements in 3914 Å emission discussed in the previous paragraph).
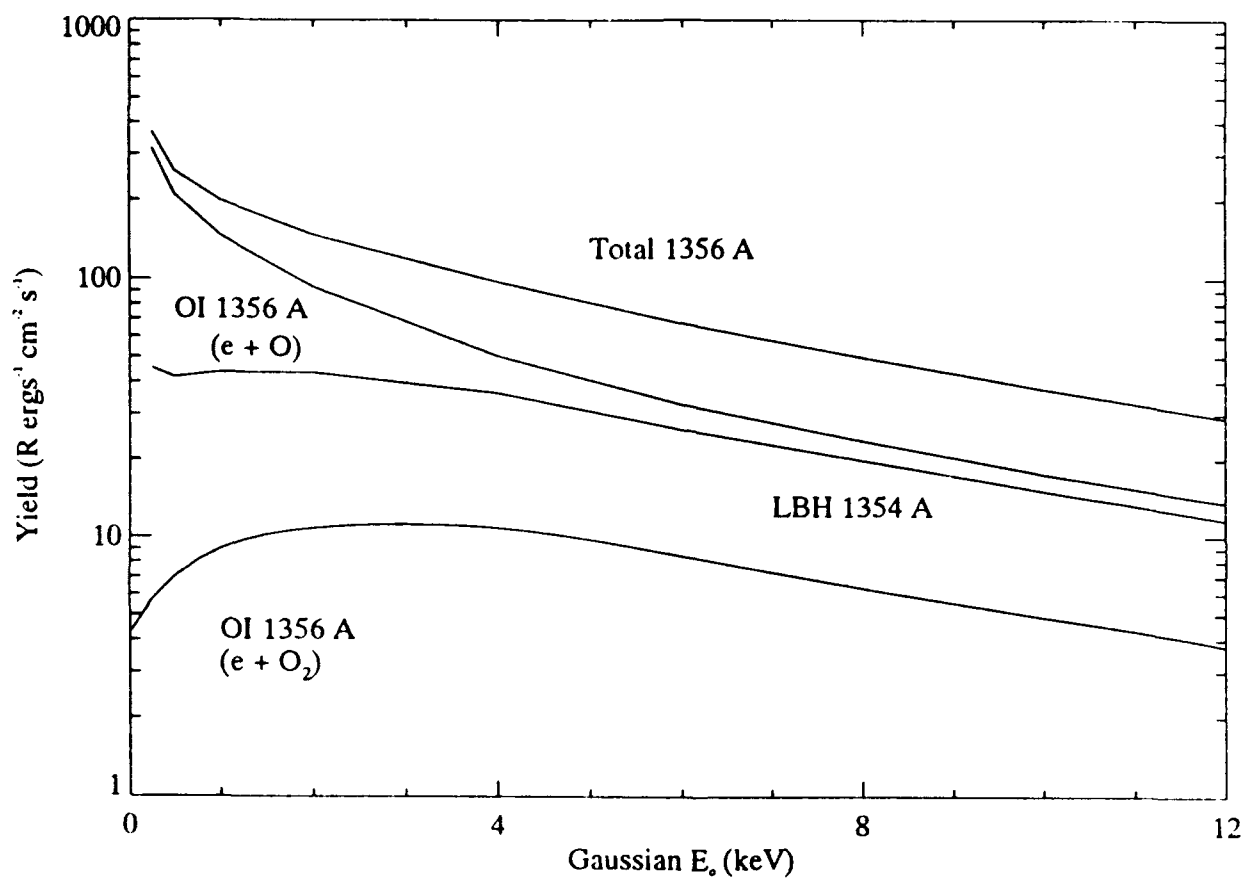
Fig. 11   The 1356 Å yield for modified Gaussian distributions broken down into its three components
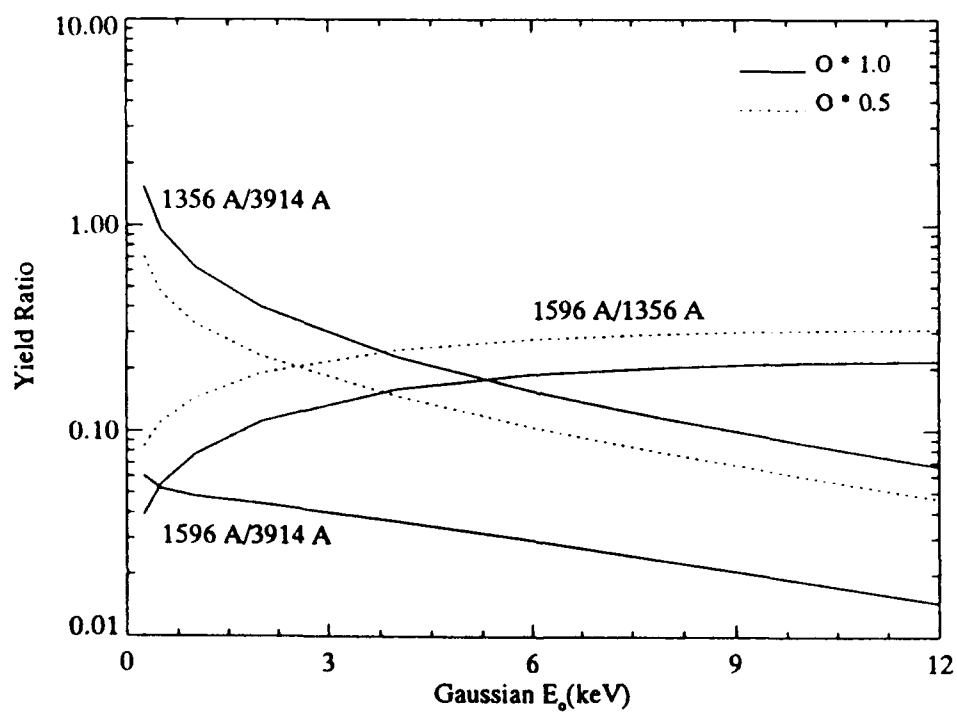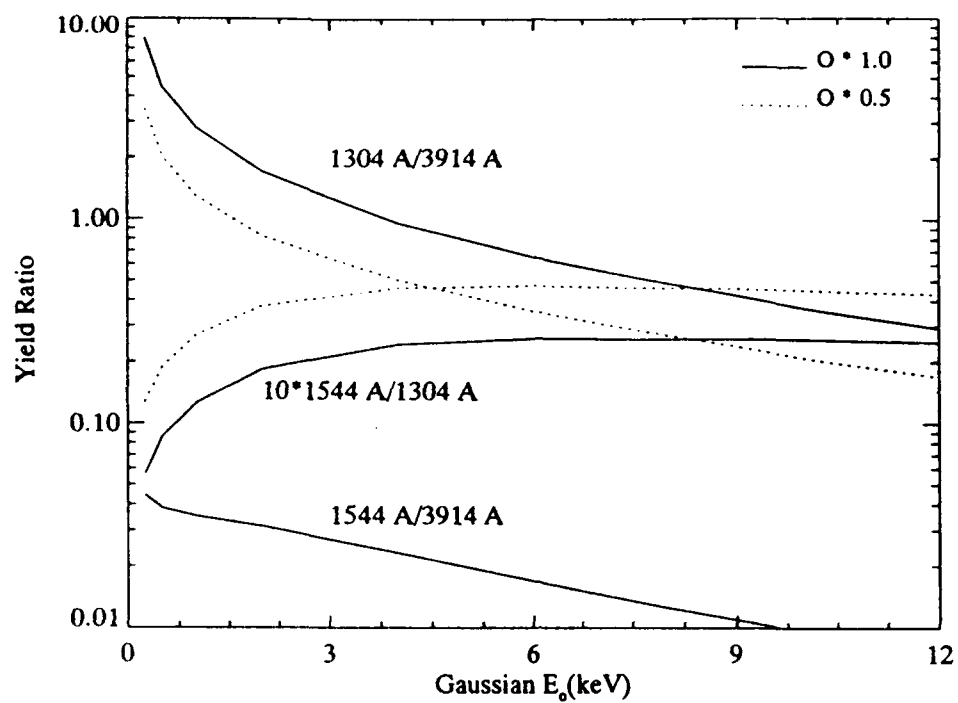
Fig. 12   Yield ratios for modified Gaussian distributions
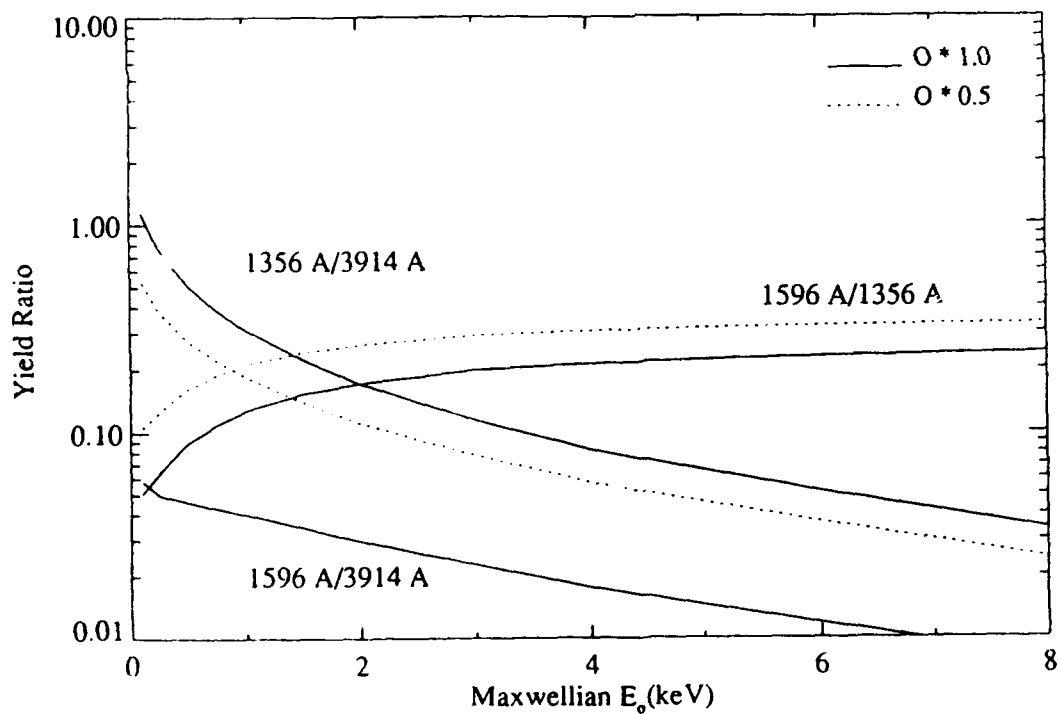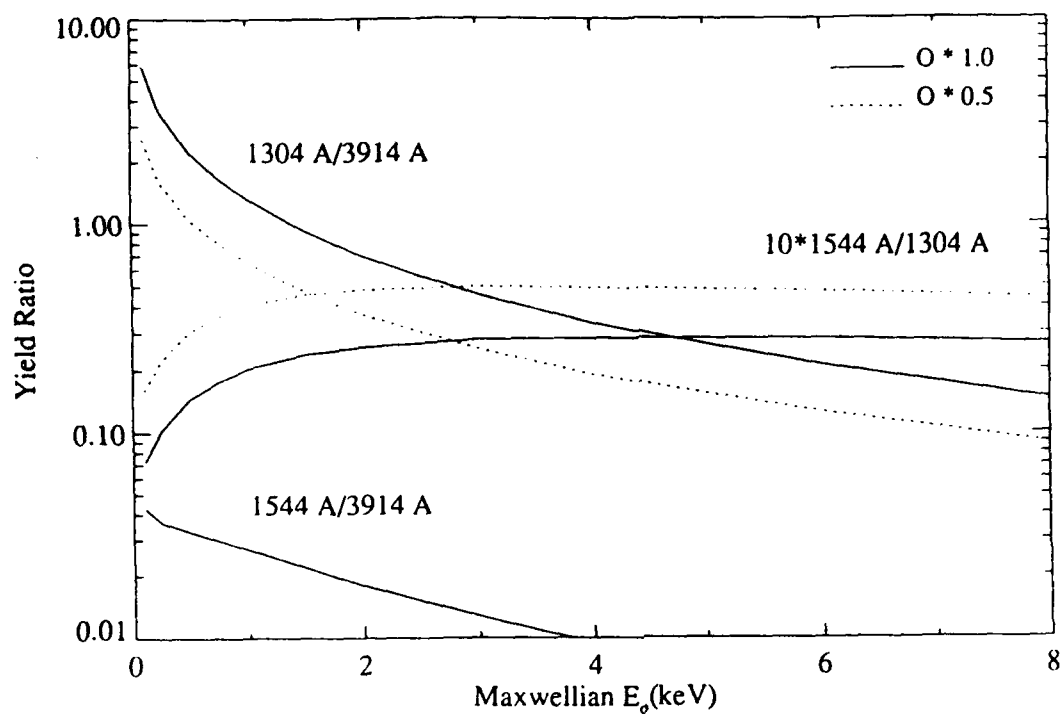
Fig. 13   Similar to Figure 12 except for modified Maxwellian distributions

5. SOURCES OF ERROR

Several sources of error affect the accuracy of the E_os and Qs deduced from the AIRS data. They are:

1. calibration errors
2. errors in cross sections
3. errors related to slant paths through spatially structured emitting regions
4. differences in fields-of-view between the FUV spectrometer and the 3914 Å photometer.
5. uncertainty in the amount of reflection at 3914 Å
6. uncertainty in the O abundance
7. uncertainty in the shape of the incident electron spectrum
8. variations within a multi-pixel data sample associated with low count rates (statistical fluctuations) and non-uniform auroral luminosity across the pixel sample

Potentially large errors in E_o and Q arise from these errors and uncertainties. Some of these, however, are expected to be small. For example, we do not believe that the systematic errors present in the calibration (item 1) or the cross sections (item 2) will be significant. Errors related to items 3 and 4 should also be small for near nadir viewing data which exhibit spatial variations on a scale comparable to or greater than the FOV of the 3914 Å photometer. Data have been selected which approximately meet these criteria.

Errors associated with items 5 - 7 are harder to quantify since we do not know the variation of albedo, O abundance, and shape of the incident electron spectrum across the observed region. We believe, however, that reasonable bounds can be placed on these variations. Within these bounds, several latitudinal profiles of E_o will be presented from the same data set. This is not done for Q since it is much less sensitive to these items.

Errors associated with item 8 are the easiest to specify since a meaningful standard deviation may be calculated. The error bars in the figures presented in the next two sections refer to item 8. The rest of this section describes how these error bars were obtained.

As noted in Section 3, north/south cuts through the images will be considered with summing in the east/west direction. Most of the results to follow have been obtained from 21 pixel mean values of the data. Uncertainty has been specified through the standard deviation (σ) of the actual distribution of counts rather than by assuming a normal distribution and taking the square root of the summed counts divided by the number of pixels. The error bars on the data presented in the next section are 2σ error bars for this actual standard deviation. It is inappropriate to assume normal statistics if there is variation in the observed aurora over the pixel sample. Efforts have been made to select north/south cuts which are reasonably uniform in luminosity over the east/west extent of swaths.

We wish to translate the 2σ error bars on the data into error bars on E_o and Q. We begin with eq. 5 which expresses the observed column emission rate $4\pi I$ as the product of Q and Y. Let us designate the needed pair of features by indices 1 and 2 and further designate $4\pi I$ by I alone. Eq. 5 for the pair of features is now

$$I_1 = QY_1(E_o) \tag{6}$$

$$I_2 = QY_2(E_o) \tag{7}$$

Let us now designate the 2σ errors in I_1 and I_2 by ΔI_1 and ΔI_2 and the corresponding errors in E_o and Q by ΔE_o and ΔQ. The latter errors may be expressed as

$$\Delta E_o = \frac{\partial E_o}{\partial I_1} \Delta I_1 + \frac{\partial E_o}{\partial I_2} \Delta I_2 \qquad (8)$$

$$\Delta Q = \frac{\partial Q}{\partial I_1} \Delta I_1 + \frac{\partial Q}{\partial I_2} \Delta I_2 \qquad (9)$$

The needed partial derivatives come from differentiating eqs. 6 and 7:

$$1 = \frac{\partial Q}{\partial I_1} Y_1(E_o) + Q \frac{dY_1}{dE_o} \frac{\partial E_o}{\partial I_1}$$

$$0 = \frac{\partial Q}{\partial I_2} Y_1(E_o) + Q \frac{dY_1}{dE_o} \frac{\partial E_o}{\partial I_2}$$

$$1 = \frac{\partial Q}{\partial I_2} Y_2(E_o) + Q \frac{dY_2}{dE_0} \frac{\partial E_o}{\partial I_2} \qquad (10)$$

$$0 = \frac{\partial Q}{\partial I_1} Y_1(E_o) + Q \frac{dY_2}{dE_o} \frac{\partial E_o}{\partial I_1}$$

Solving for the four derivatives, we find:

$$\Delta E_0 = \frac{Y_2 \Delta I_1 + Y_1 \Delta I_2}{|Y_1' Y_2 - Y_2' Y_1|}$$

$$\Delta Q = \frac{Y_2' \Delta I_1 + Y_1' \Delta I_2}{|Y_1' Y_2 - Y_2' Y_1|} \qquad (11)$$

where

$$Y_1' = \frac{dY_1}{dE_o} \ , \quad Y_2' = \frac{dY_2}{dE_o} \tag{12}$$

Numerical values of the derivatives are obtained from the slopes of the theoretical yield curves presented in the previous section.

6. DATA AND DATA RATIOS

The brightnesses of the emissions observed and their ratios are used to deduce Qs and E_os. Summing several pixels is necessary for both LBH channels since there are typically only a few counts per pixel unless Q for that pixel becomes large (e.g. > 10 ergs $cm^{-2}s^{-1}$). Our approach is to select north/south cuts through the central portions (near vertical viewing) of the images. The selected swaths contain bright emission but have minimal variation in the east/west direction over the chosen widths of these cuts. We would like these swaths as wide as possible to improve the counting statistics in the LBH channels. Results will be shown for widths of 5, 11, and 21 pixels (22 km, 55 km, and 110 km at an emission height of 110 km) centered on the same vertical cut. The degree of variation in the data from one width to another will indicate when it is valid to average over the preferred 21 pixel width. Data and results now follow by pass starting with the Jan 29 pass.

6.1   Jan 29 pass (1356 Å, 1596 Å, 3914 Å)

We have chosen a north/south cut centered at horizontal pixel #100 which is to the east of the satellite track (see plate 1). The viewing angle at this pixel is about 25° from nadir. The corresponding range of angles, ten pixels to either side, is 21° to 29°. The averaged data along this cut from the three images (at 1356 Å, 1596 Å, 3914 Å) are shown in Figure 14 versus geographic latitude from 56° to 67°. The three curves in each panel come from widths of 5, 11, and 21 pixels and averaging in the north/south direction over 3 pixels. In general, there is little difference between the narrowest (5 pixels) and widest (21 pixels) swaths at 1356 Å and 3914 Å. The exception occurs between 62° and 63° latitude at 1356 Å where the difference is as great as about 25%. This does not occur at 3914 Å and is probably due to differences in fields-of-view (discussed in Section 2), suggesting greater north/south structure than at other latitudes. Greater differences in the data between swath widths occur at 1595 Å. Since 1356 Å does not show such differences, this can be attributed to statistical fluctuations. The 3914 Å data are around 20 kR over about 2° in latitude. This corresponds to significant energy deposition over
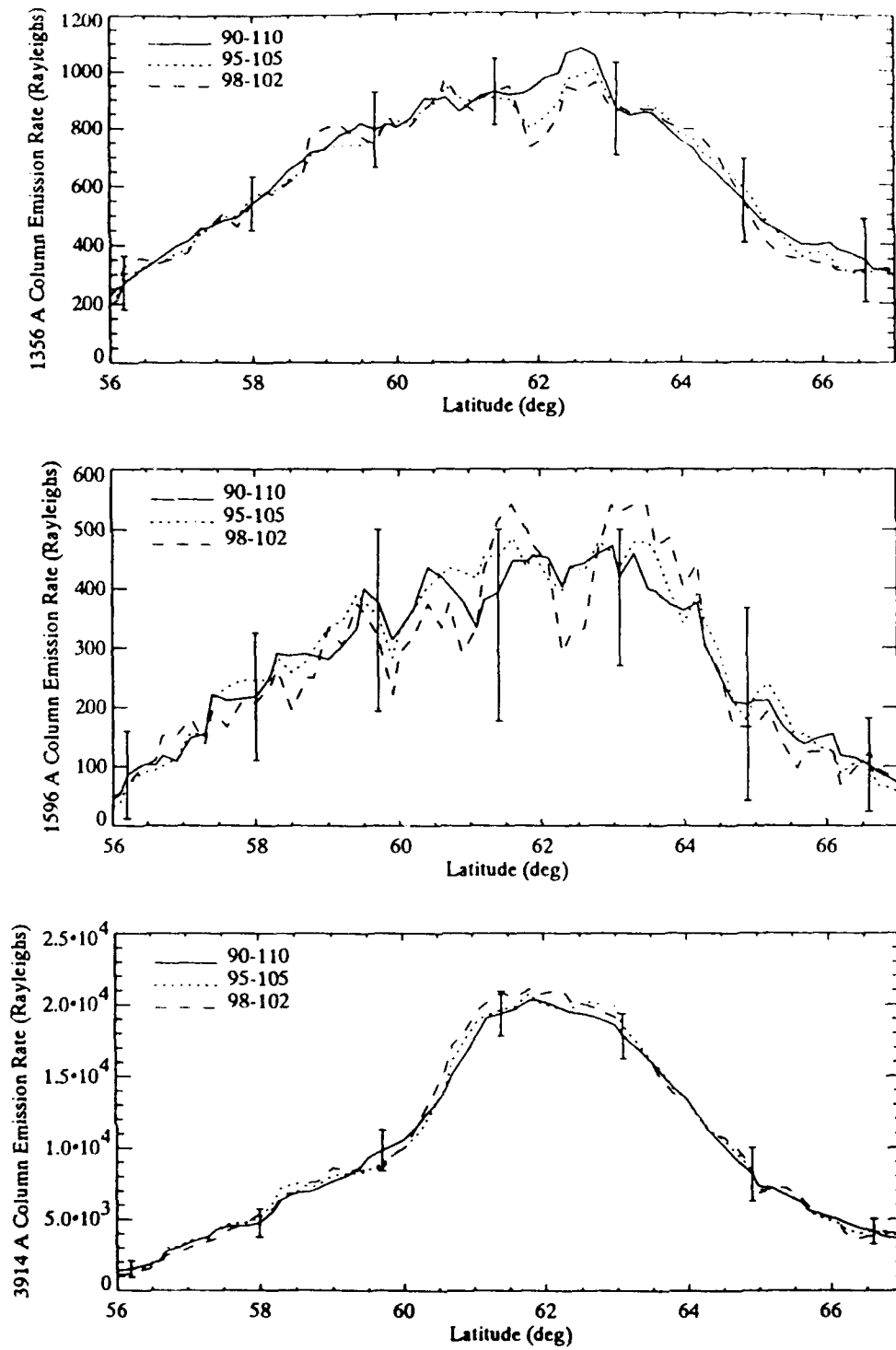
Fig. 14   Data versus geographic latitude from Jan 29 pass. Each panel shows emission profiles averaged in the east/west direction over 5, 11, and 21 pixels, all centered on horizontal pixel 100. The error bars (2σ) refer to the 21 pixel wide profiles and were obtained from the actual distributions of counts as discussed in Section 5

a large region and could produce interesting dynamical effects depending on the duration of the deposition.

Ratios of the data are shown in Figure 15. The 1356/3914 ratio (upper panel) is the smoothest due to good counting statistics at both wavelengths compared to LBH 1596 which is present in the other two ratios. The 1356/3914 ratio varies more than a factor of three and is smallest at 62° where energy deposition is largest. This ratio and the data are anticorrelated, see Figure 14. This suggests some degree of correlation between Q and E_o, which will be examined in the next section. For precipitation in discrete arcs, correlation is expected based on our present understanding of the origins of this precipitation (see, e.g., Lyons, 1981). Some of the variation in the 1356/3914 ratio may come from changes in the O concentration and in the Rayleigh backscattering and reflection. Since we do not know the extent of these effects for the given cut across the auroral oval, E_o profiles will be shown for O concentrations and 3914 Å albedos spanning the likely range of uncertainty in these parameters. One other possible source of variation not to be attributed to changes in E_o is spatial structure on the scale of the FOV. We assume in this analysis that the small difference between the 1356 Å and 3914 Å FOV*s* is unimportant.

If the counting statistics at 1544 Å were comparable to 1356 Å, the 1596/3914 Å ratio shown in the middle panel of Figure 15 would be preferable to the 1356/3914 ratio for estimating E_o for characteristic electron energies above a few keV. Both ratios have about the same degree of variation above a few keV for a given set of neutral density profiles due to similar photoabsorption cross sections at 1356 Å and 1596 Å (see Section 4). For the 1596/3914 ratio, both emissions arise from electron impact on N_2 and are independent of O concentration changes. Therefore, the 3914 Å albedo is the main uncertainty affecting the accuracy of E_o, assuming good relative calibration between 1596 Å and 3914 Å. In spite of poor counting statistics, we see similar behavior between the 1596/3914 and 1356/3914 ratios in Figure 15. Differences at the low and high latitude ends are attributed to worsening counting statistics at 1596 Å, and especially at the low latitude end, to E_o values less than a few keV, for which the two yield ratios have different shapes. Both ratios to the right of their minima suggest larger E_o*s* than to the left
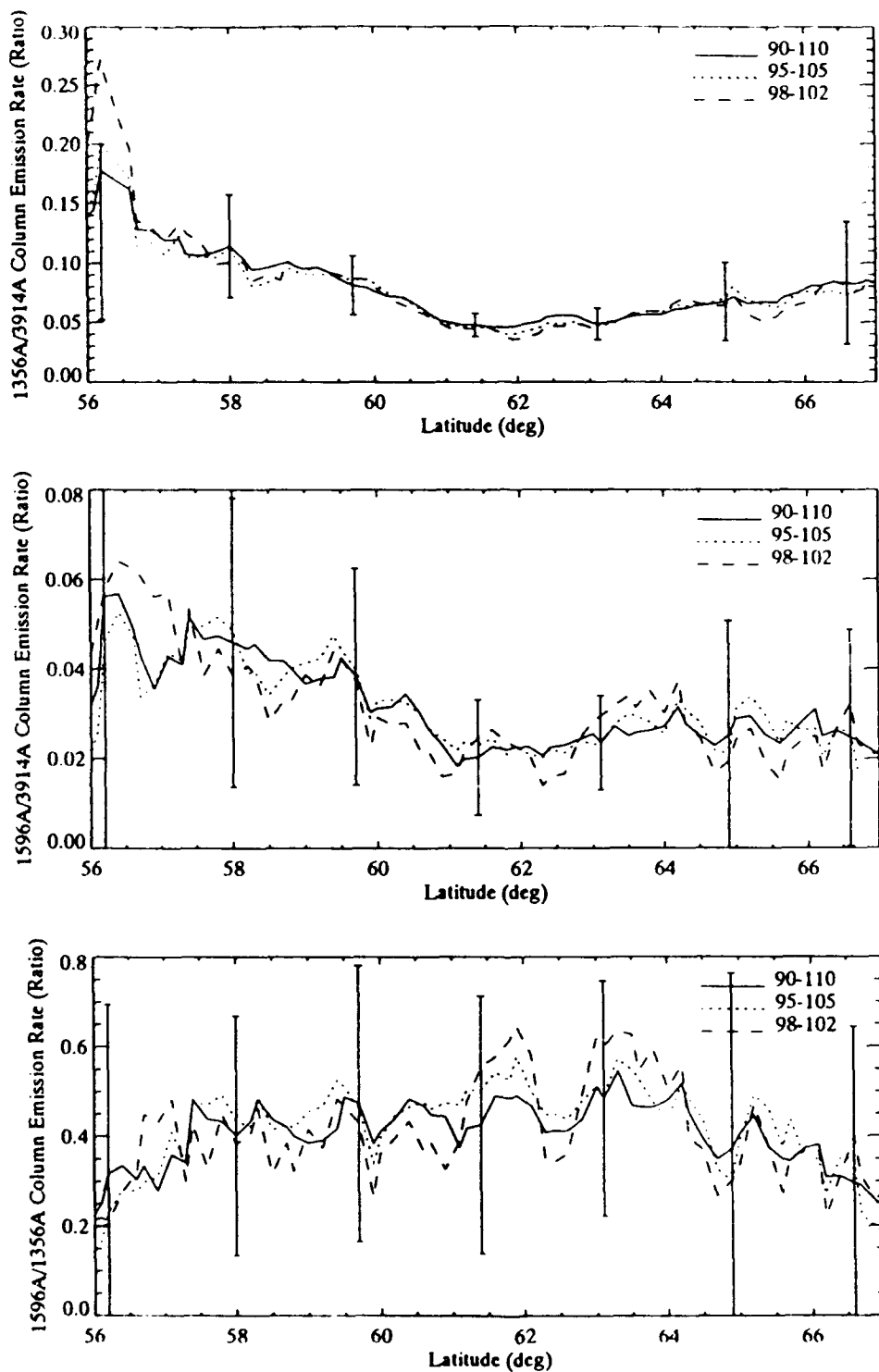
Fig. 15   Data ratios versus latitude corresponding to the data in Figure 14. Similar to
Figure 14, the error bars refer to the 21 pixel wide profiles

although each ratio presents a different trend in E_o. The trend based on the 1596/3914 ratio is little or no overall E_o variation from 63° to 67° whereas a decrease is suggested from the 1356/3914 ratio. This could be explained by an increase in the O abundance away from the region of maximum energy deposition in combination with low 1596 Å counting statistics.

The last ratio to be discussed in Figure 15 is 1596/1356 appearing in the bottom panel. The high frequency structure as well as that in the middle panel is mostly statistical. It cannot be attributed to either changes in the O concentration or to changes in E_o when taking into account the relatively unstructured 1356/3914 data and the fact that the 1596/1356 ratio varies slowly with E_o above a few keV. The low frequency structure is likely non-statistical showing a gradual rise and than decrease from low to high latitudes. Given the weak variation with E_o, the dominant cause is likely to be composition changes. The overall shape suggests greater O densities at the low and high latitude ends where less energy deposition is occurring. This is further supported on the high latitude end by the differences between 1356/3914 and 1596/3914 in this region discussed above. Based on these observations, the value of 1596/1356 in this analysis is to monitor large scale variations in O.

6.2   Jan 12 pass (1304 Å, 1544 Å, 3914 Å)

A briefer discussion of Jan 12 pass data will follow since many of the observations made above apply here as well. The same procedure used on Jan 29 pass data was followed for selecting north/south cuts through the 1304 Å, 1544 Å, and 3914 Å images. The results are shown in Figure 16 from 52° to 62° N latitude. The central pixel number for the three swaths is 160 giving a look angle of 1° east of nadir. The range of angles is -2.8° to 5.2° over the 21 pixel width swath. On this pass, the observed portion of the auroral oval is about 3° south compared to the Jan 29 pass. The maximum brightness, however, occurs near the same latitude. Good uniform brightness occurs across the 21 pixels based on the similarity between the three curves for either 1304 Å or 3914 Å. Again, we are dealing with low counts for the LBH channel (1544 Å) as was the case for the LBH 1596 Å channel.
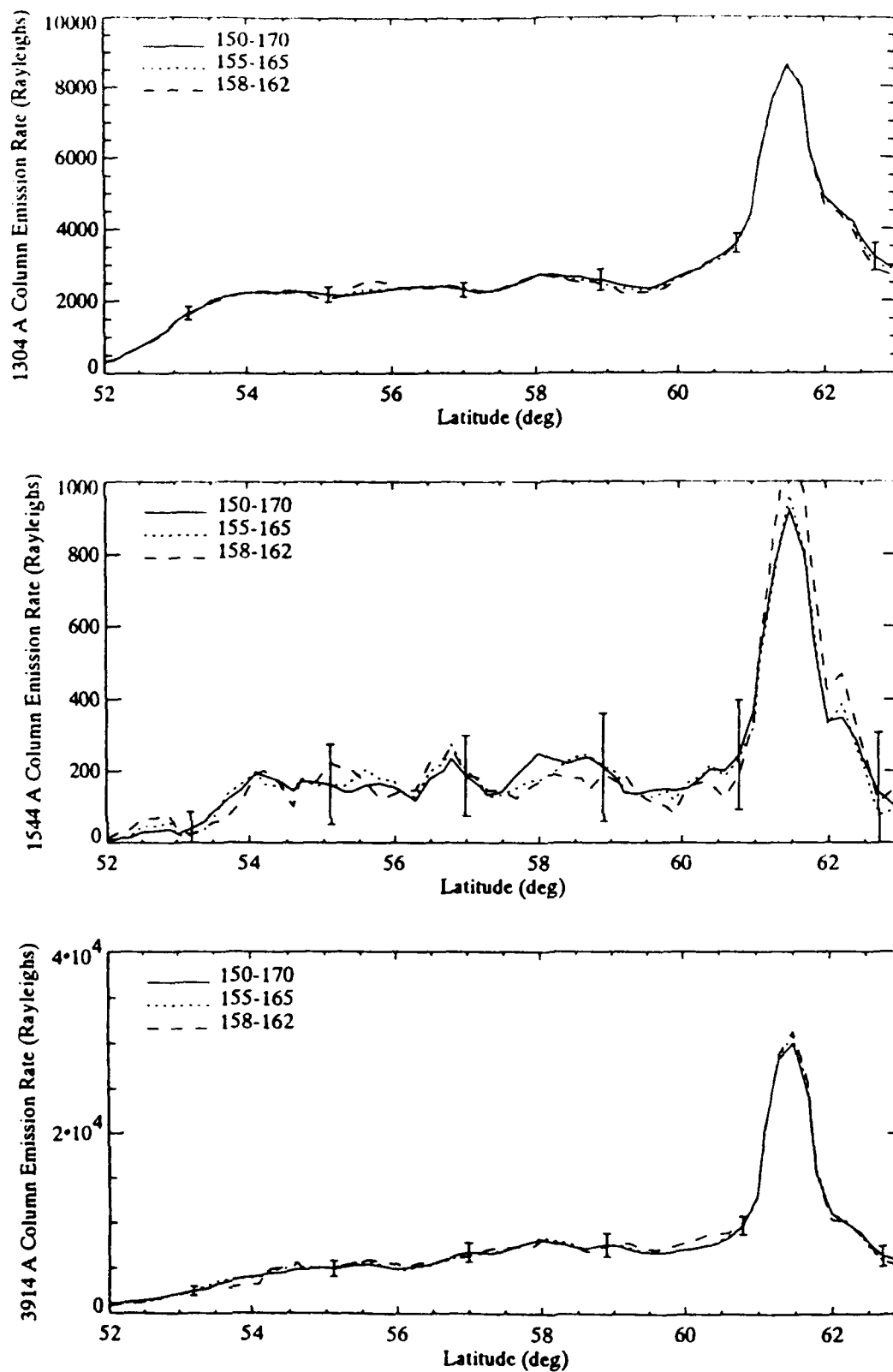
Fig. 16   Similar to Figure 14 except for the Jan 12 pass

Ratios of the data are given in Figure 17. Like the corresponding ratios from the Jan 29 pass, the 1304/3914 and 1544/3914 ratios are most useful for estimating E_o while the 1544/1304 ratio can serve as a monitor to changes in O. Like the 1596/1356 ratio, 1544/1304 shows little variation with E_o above a few keV but is sensitive to changes in O. Like 1356/3914 and 1596/3914, the 1304/3914 and 1544/3914 ratios behave similarly above a few keV (see the upper and middle panels of Figure 17). This similarity is difficult to see because of the statistical fluctuations in 1544/3914. The decrease is seen in the 1544/3914 ratio from 54° to 60° can also be seen in the 1304/3914 ratio. In spite of these fluctuations, we will determine E_o from 1544/3914 in the next section and compare it with that obtained from 1304/3914. Overall, the agreement will be seen to be surprisingly good.
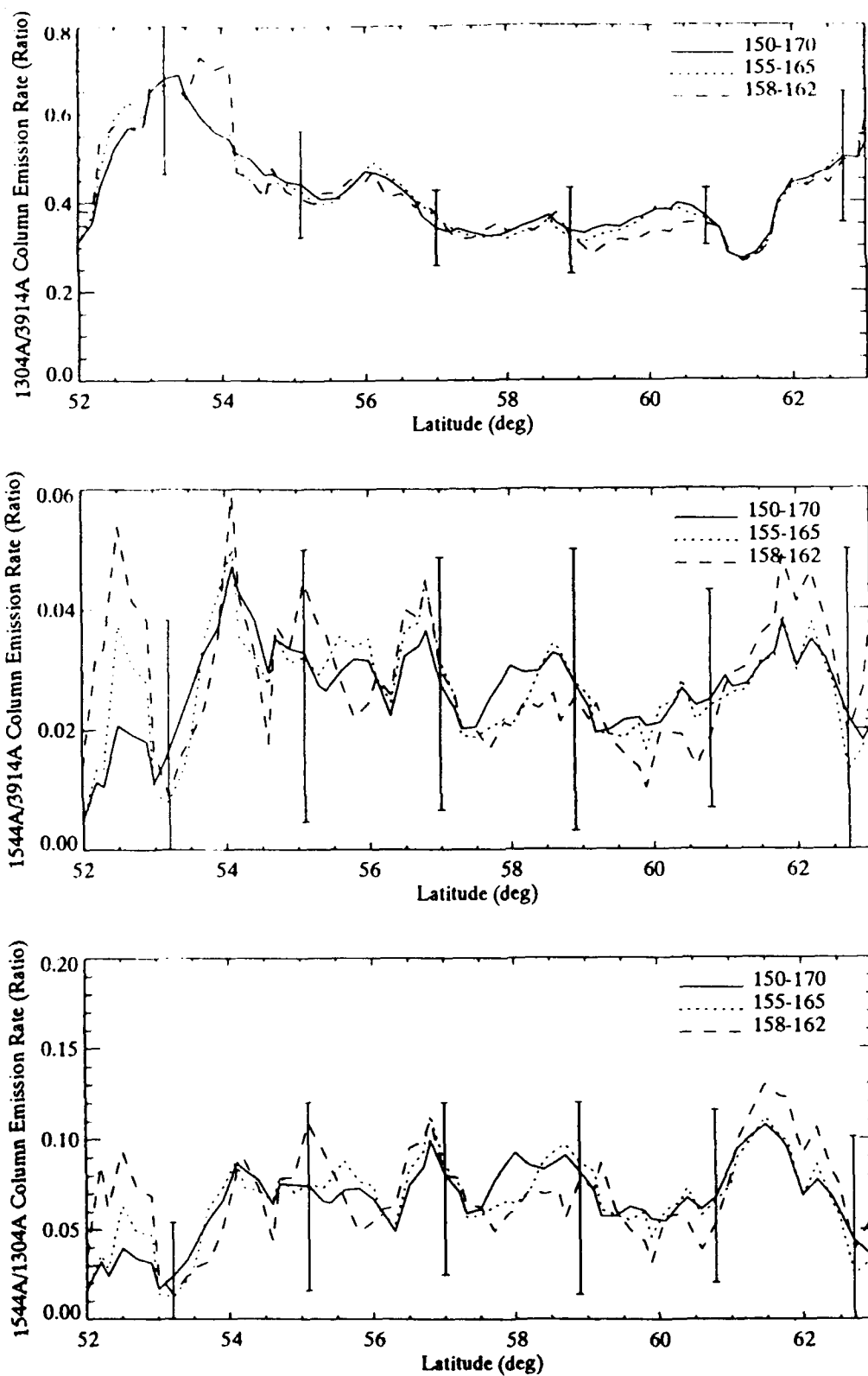
Fig. 17   Data ratios versus latitude corresponding to the data in Figure 16

7. Q and E_o

Inferred electron precipitation characteristics in the form of Q and E_o follow for the data presented in the previous section. For each pass, several E_o profiles versus latitude will be presented to show the sensitivity of E_o to O, the 3914 Å albedo, the assumed electron energy distribution (Gaussian vs. Maxwellian), and the applied data ratio (1356/3914 vs. 1596/3914 for the Jan 29 pass and 1304/3914 vs. 1596/3914 for the Jan 12 pass).

7.1   Jan 29 pass

We begin with Q obtained from the 21 pixel averaged 3914 Å data in Figure 14. The applied yield curve comes from Figure 9 for Gaussian energy distributions with O scaled by .5. To account for albedo, the yield curve was scaled by 1.2 and 1.4 leading to the two Q profiles in Figure 18. To apply the scaled yield curves, E_o was first determined from the 21 pixel averaged 1356/3914 data ratio to be further discussed below. This is not a critical step since the 3914 Å yield curve is nearly constant with E_o except below about 1 keV. Figure 18 shows that substantial energy deposition occurred over several degrees of latitude centered on 62°. Referring back to Figure 5, the three hour index a_p is about 40 which signifies a moderately disturbed time. For the high level of energy deposition shown in much of Figure 18, discrete aurora is present. For this reason, most of the E_o profiles to follow were obtained with Gaussian yields.

The upper panel in Figure 19 shows E_o obtained from the 5, 11, and 21 pixel averaged 1356/3914 data in Figure 15. The applied yield ratio comes from Figure 12 with O scaled by .5 and was divided by 1.2 to account for albedo at 3914 Å. Significant east/west structure over the 21 pixel swath is seen to be limited to three localized regions near 56°, 62°, and 65.5°. The lower panel shows similar results except using the Maxwellian 1356/3914 yield ratio from Figure 13 reduced by 1.2 for albedo and with O scaled by .5. The shapes of the E_o profiles are similar between the two panels but differ in magnitude by about a factor of two. This is consistent with the definitions of E_o for the two types of distributions.
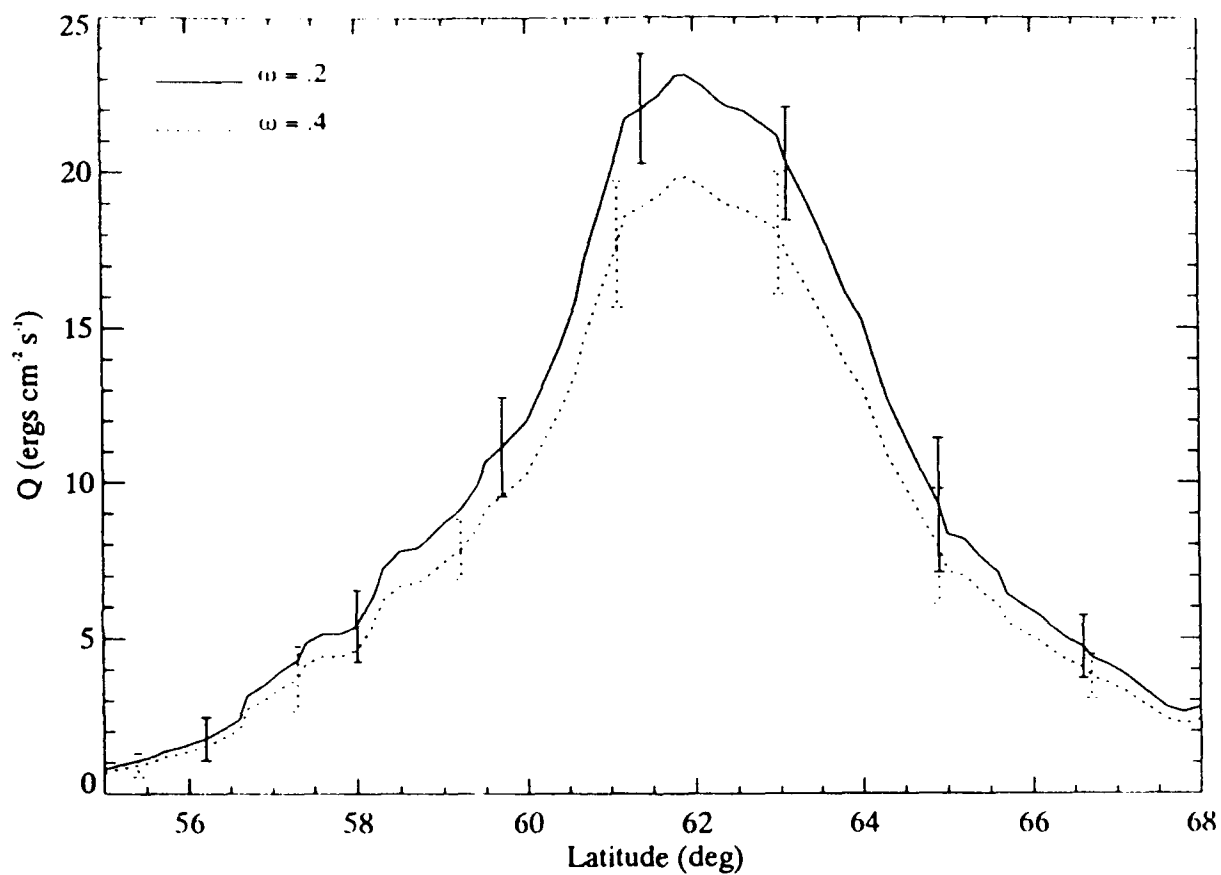
Fig. 18   Energy flux Q versus latitude for Jan 29 pass based on the 21 pixel averaged 3914 Å data in Figure 14 and the 3914 Å yield curve in Figure 9. Results are shown for scalings of the yield curve by 1.2 and 1.4 corresponding to albedos of .2 and .4. The error bars were obtained from eq. 11 in Section 5
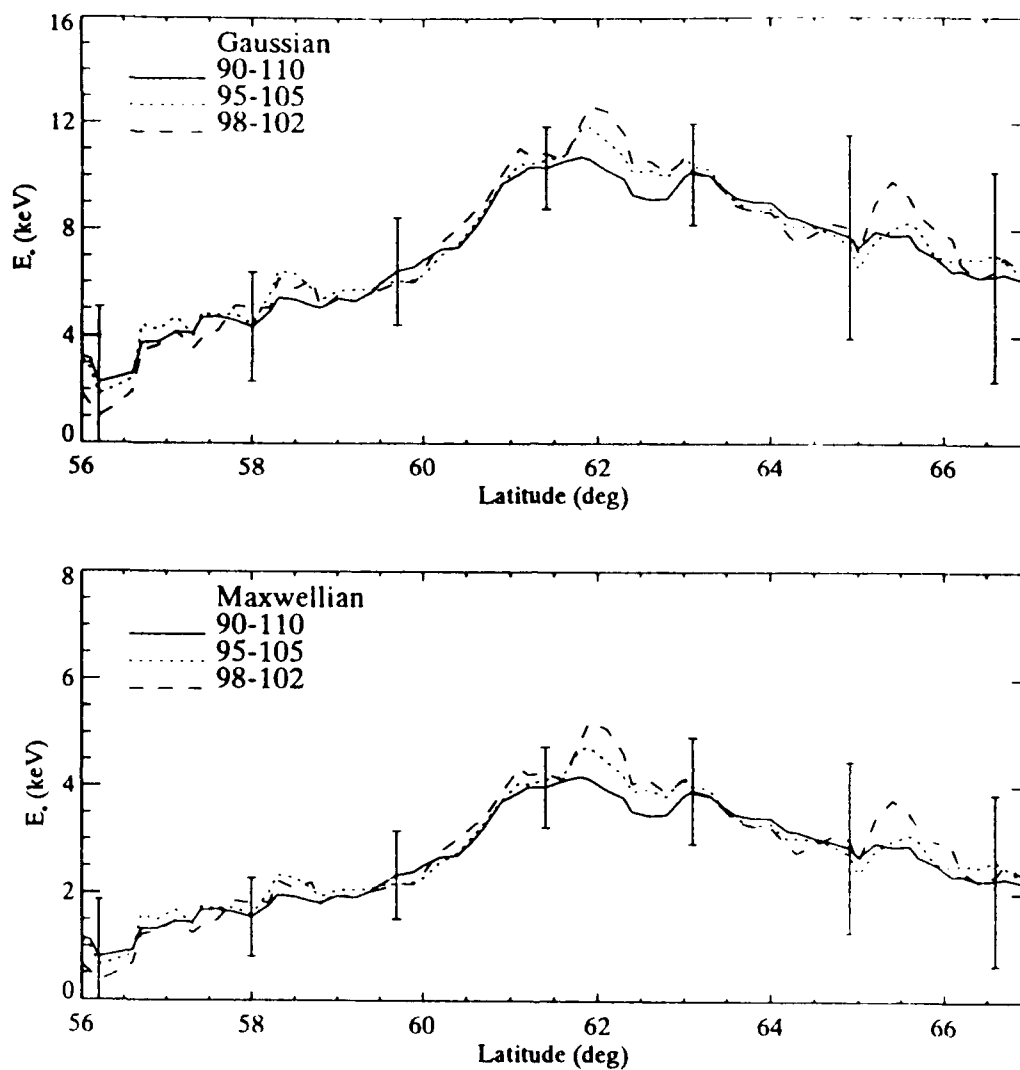
Fig. 19 E_0 versus latitude for Jan 29 pass based on the 1356/3914 data ratios in Figure 15 and the 1356/3914 yield ratios in Figures 12 and 13 for O scaled by .5. The yield ratios were divided by 1.2 to account for an albedo of .2 at   14 Å. The error bars were obtained from eq. 11 in Section 5

The sensitivity of E_o to the O concentration, the 3914 Å albedo, and applied data ratio is shown in Figure 20 for the 21 pixel averaged data. The upper panel shows the sensitivity to O using the 1356/3914 data ratio. A decrease of about 3 keV results from scaling the O density profile by .5. The change is not in direct proportion to O due to contributions to 1356 Å from LBH 1354 Å (see Figure 11). By contrast, E_o based on 1596/3914 is essentially independent of O but is suffers from low count rates at 1596 Å (further discussion below).

The middle panel shows two E_o profiles for O scaled by .5 with 3914 Å albedos of .2 and .4 using the 1356/3914 data ratio. These albedos were chosen as approximate lower and upper limits to changes brought about by changing luminosity patterns across the sky and changing cloud and surface conditions. A decrease of about 15% arises from increasing the albedo from .2 to .4.

The lower panel compares $E_o s$ obtained from 1356/3914 and 1596/3914 data. The 1356/3914 E_o comes from the upper panel with O scaled by .5. The 1596/3914 data and yield ratio curve come from Figures 15 and 12, respectively, with the yield ratio divided by 1.2. The 1596/3914 E_o values below 60° are unphysical and arise in a region of softer precipitation. Compared to 1356/3914, the 1596/3914 yield ratio is insensitive to E_o at low energies and can lead to large errors for soft precipitation given even modest errors in the applied magnitude of the yield ratio curve. This applies as well to small systematic and statistical errors in the measured intensity ratio.

In the region of strong, hard precipitation (approximately 60° to 64° latitude), the two curves possess approximately the same shape but differ by about 3 to 4 keV in magnitude. The likely causes are errors in the assumed O concentration and modest errors in cross sections and calibration.

Above 64°, the trends are different and, as discussed in the previous section, may be caused in part by an increase in O (and in part by statistical fluctuations). The increase has no effect on E_o obtained from 1596/3914 data but will lead to underestimated E_o values from
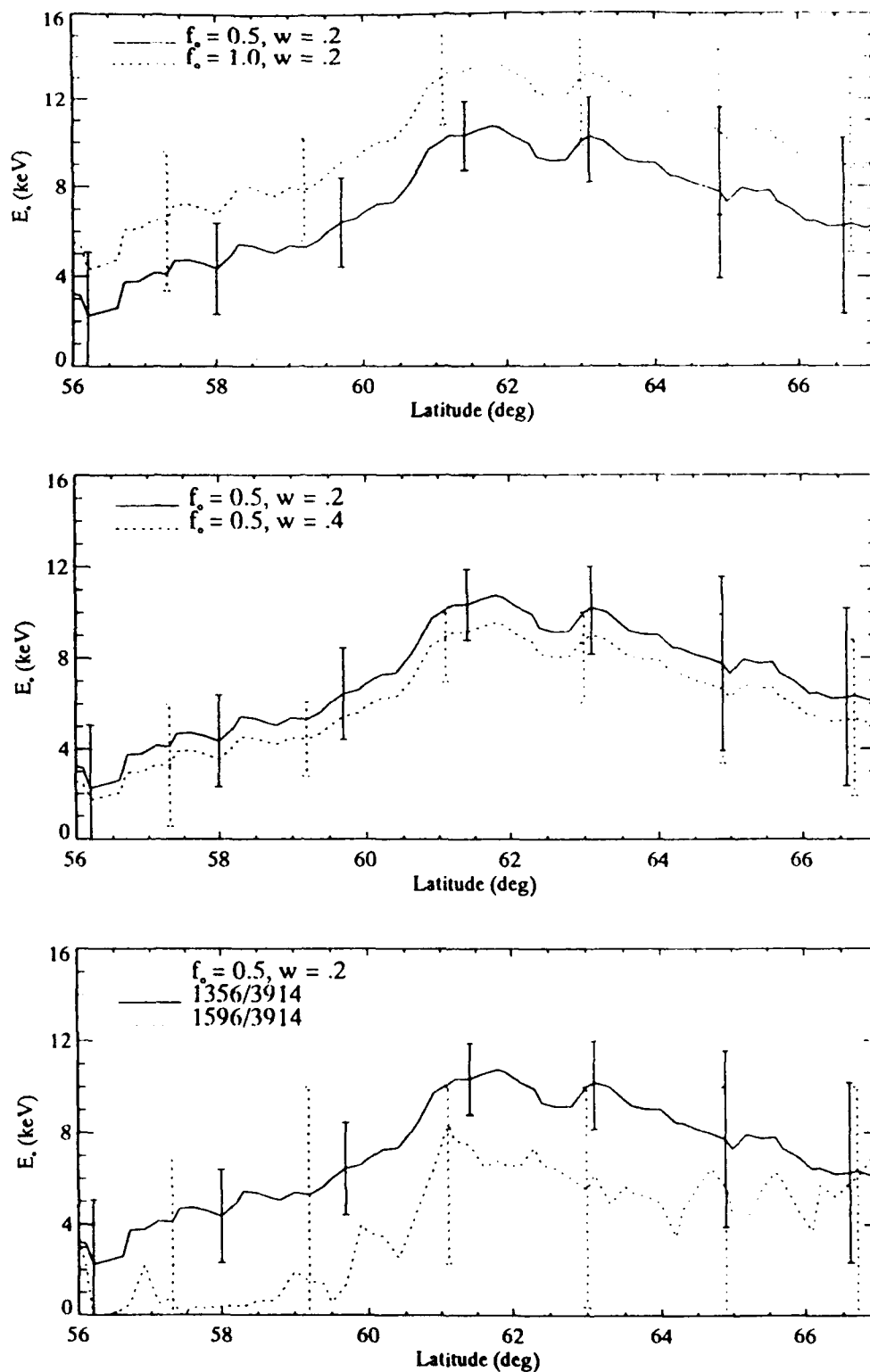
Fig. 20 E_o versus latitude for Jan 29 pass showing sensitivity to the O concentration (upper panel), 3914 Å albedo (middle panel), and data ratio (lower panel). The solid curve in each panel is the 21 pixel averaged E_o profile from the upper panel of Figure 19

1356/3914 data if the O concentration is higher than assumed in the derivation of the corresponding yield ratio (see Figure 12 for the dependence of this yield on O).

E_o is seen to range from about 3 to 10 keV which is within the range expected for the level of auroral activity recorded. There is also a correlation with Q which is expected if discrete aurora is present. More will be said about this in Section 9.

7.2   Jan 12 pass

The energy flux Q corresponding to the 21 pixel averaged 3914 Å data in Figure 16 is shown in Figure 21. The same yield curves used to obtain the Qs for the Jan 29 pass were used here. Referring back to Figure 5, the index a_p achieved a value of 22 during the observations reflecting a less disturbed time than for the Jan 29 pass. Overall energy deposition is less for this cut than that of the Jan 29 pass but with greater maximum deposition which reaches about 30 ergs $cm^{-2}s^{-1}$ at 61.5° latitude.

Paralleling the results for the Jan 29 pass, Figure 22 gives E_o profiles for 5, 11, and 21 pixel wide swaths centered on the same north/south cut for Gaussian and Maxwellian yield ratios. The results were obtained with the 1304/3914 data in Figure 17 and corresponding yield ratios from Figures 12 and 13 with O scaled by .5. Surprisingly, only a modest increase in E_o occurs between 61° to 62° in spite of a large increase in Q.

Sensitivity of E_o to O, albedo, and applied data ratio is shown in Figure 23. The upper panel shows sensitivity to O using the 1304/3914 Å data ratio. More than a factor of two reduction occurs for scaling O by .5 which reflects the sensitivity of the 1304 Å yield curves in Figures 9 and 10 to O. Greater changes occur at 1304 Å compared to 1356 Å due to multiple scattering effects. The exhibited sensitivity shows that 1304/3914 data should be avoided for inferring E_o without knowledge of the O abundance but will be effective for inferring this abundance with independent information on E_o.
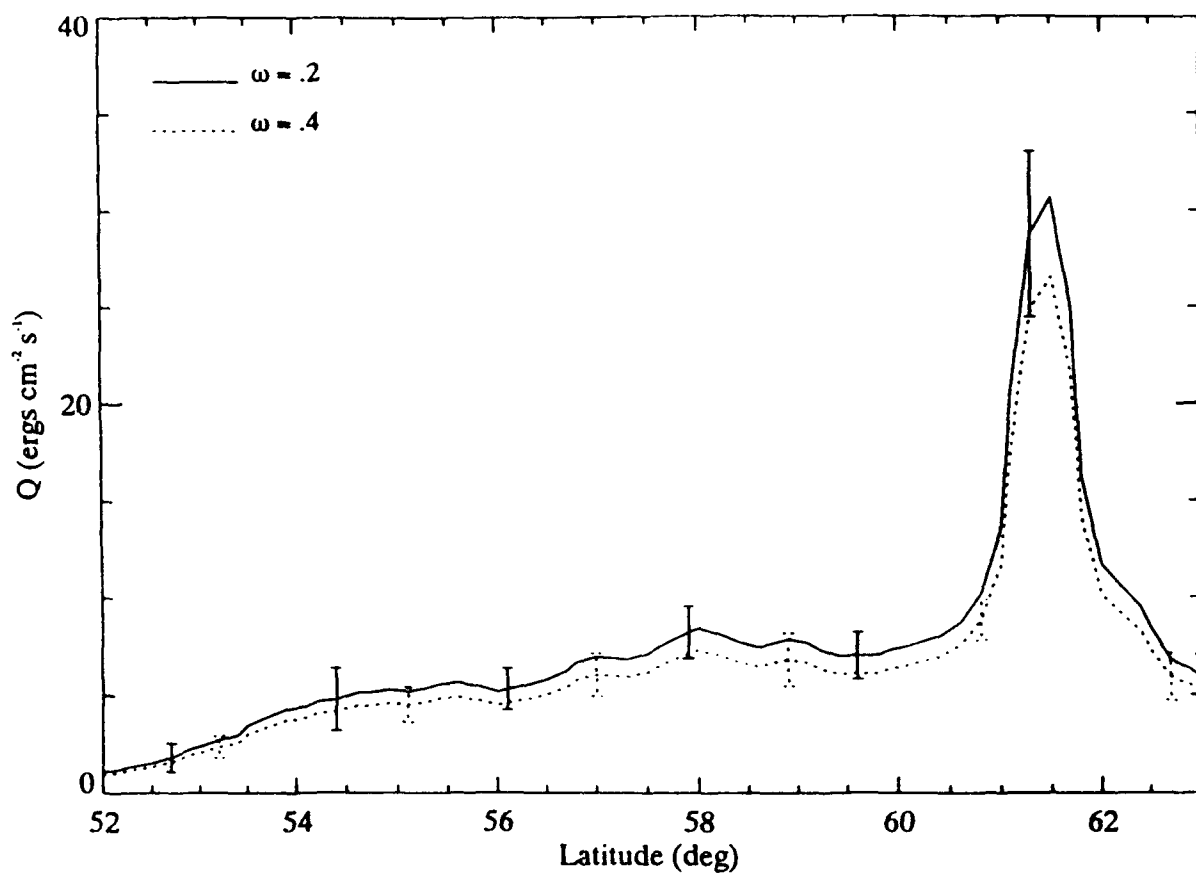
Fig. 21   Similar to Figure 18 except for the Jan 12 pass based on the 21 pixel averaged
3914 Å data in Figure 16
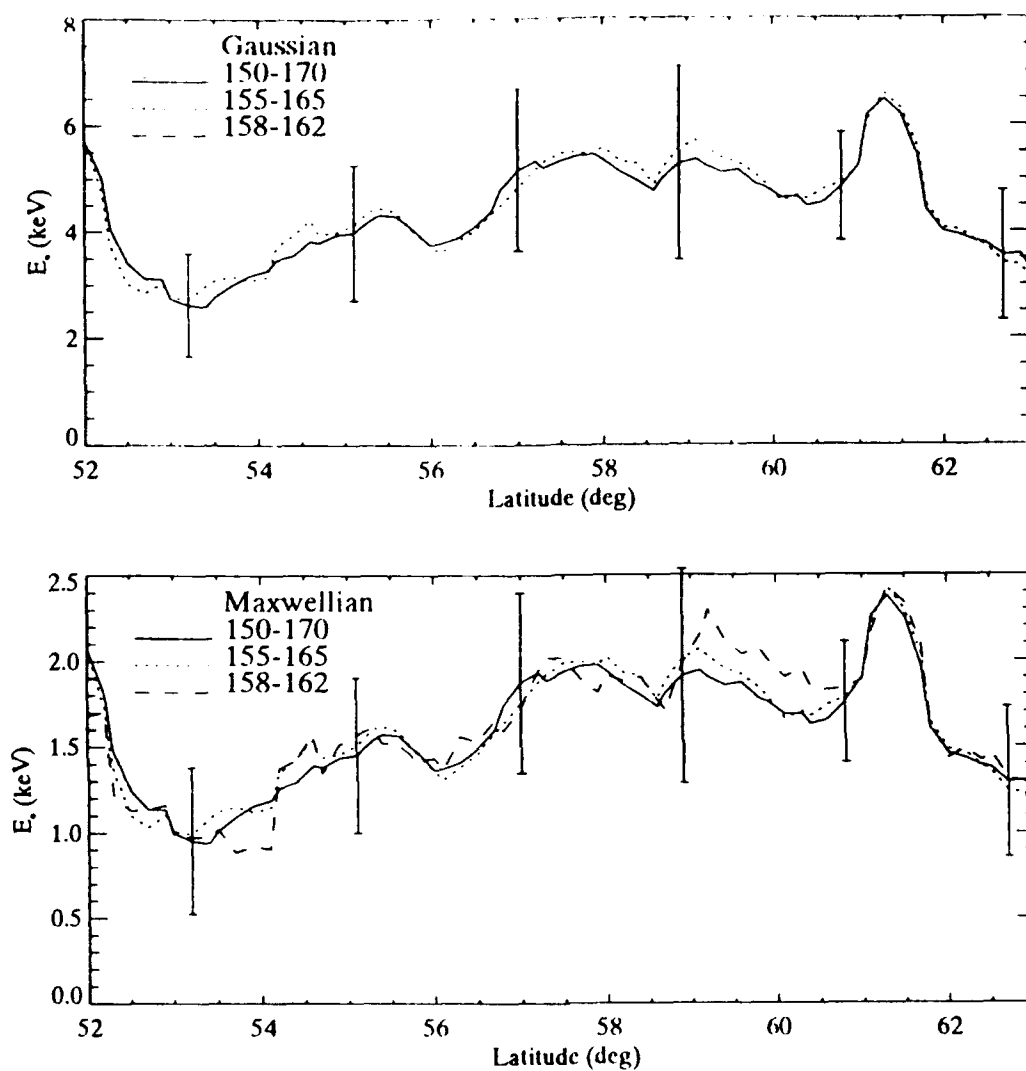
Fig. 22   Similar to Figure 19 except for the Jan 12 pass based on the 1304/3914 data ratios in Figure 17
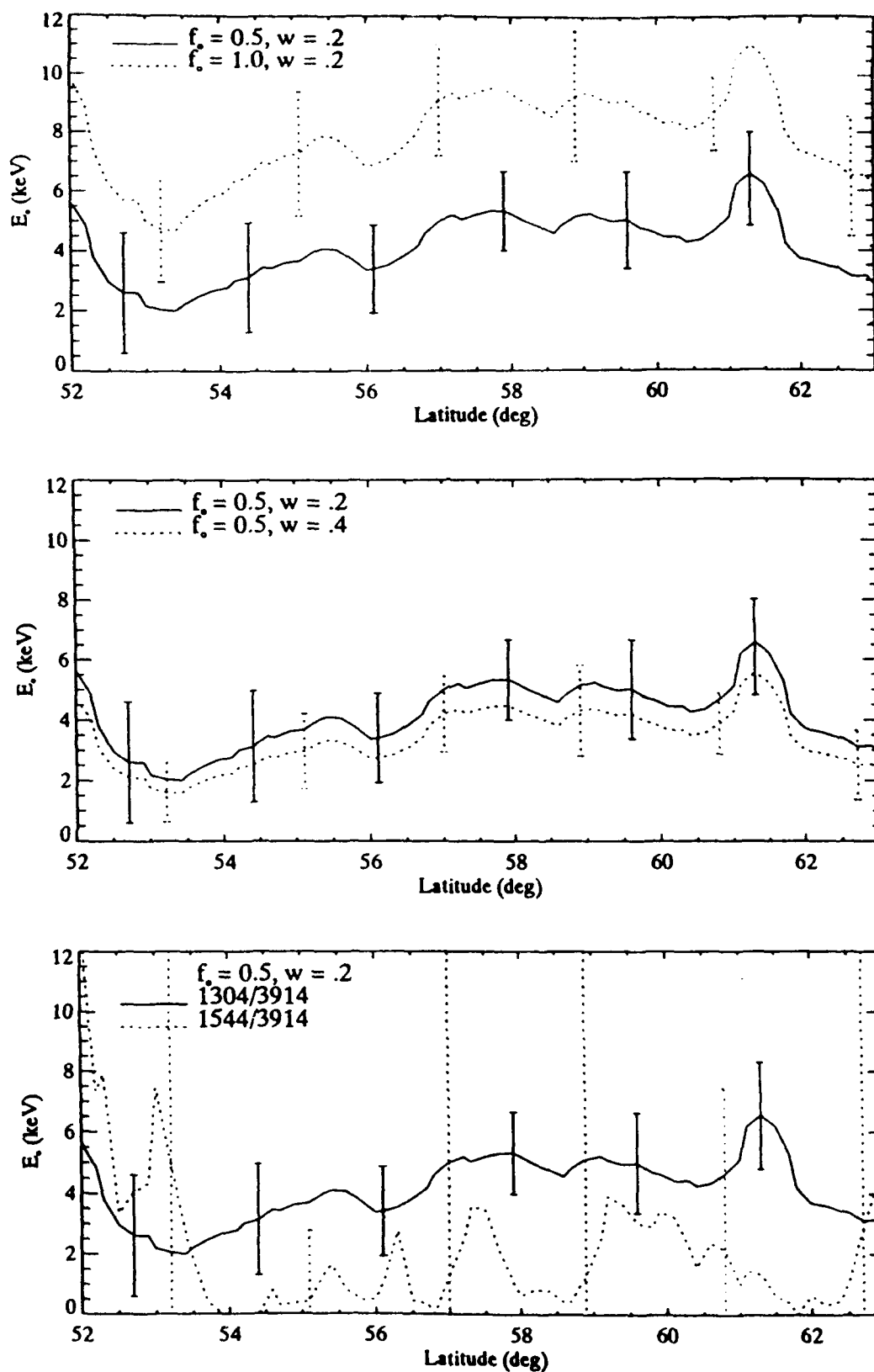
Fig. 23   Similar to Figure 20 except for the Jan 12 pass based on the 21 pixel averaged
           data ratio in Figure 17

The middle panel shows sensitivity to albedo using 1304/3914 data with O scaled by .5. The exhibited changes are similar to those in Figure 20 based on 1356/3914 data. The lower panel compares E_o obtained from 1304/3914 and 1544/3914 data. Similar to the comparison using 1356/3914 and 1596/3914 data, smaller E_o values are inferred using N_2 in place of O emission in the numerator of the data ratio. The same sources of error apply here with more weight given to uncertainties in O and to statistical errors due to fewer counts available at 1544 Å compared to 1596 Å. Fewer counts arise from a combination of the 1544 Å region being relatively less bright compared to the 1596 Å region (see Figure 4) and less overall energy deposition seen on the Jan 12 pass compared to the Jan 29 pass. Beyond these issues, the 1544/3914 data ratio is simply not adequate for obtaining E_o where soft precipitation is occurring. Relatively large changes in E_o where E_o is small produce little change in the ratio due to weak pure absorption of the LBH emission by O_2.

8. $N_{max}E$ and $h_{max}E$

8.1 Jan 29 pass

Figure 24 gives $N_{max}E$ (upper panel) and $h_{max}E$ (lower panel) for the four inferred sets of incident electron spectra from the previous section based on the 1356/3914 data ratio. Results are not included for the 1596/3914 data ratio because of the problems discussed in the previous section. $h_{max}E$ was obtained by interpolation using the precomputed $h_{max}E$, E_o relationships previously shown in Figure 4. (The dependence of $h_{max}E$ on Q is weak enough to be ignored.) $N_{max}E$ was obtained by bilinear interpolation using precomputed values as functions of both E_o and Q. Its dependence on Q is nearly proportional to the square root of this quantity. A time dependent chemistry model was used to obtain the EDPs from which the precomputed $N_{max}Es$ and $h_{max}Es$ were obtained. The duration of energy deposition was chosen to be ten minutes at which point the EDP at E region altitudes is essentially in chemical equilibrium.

Three pairs of profiles are shown for inferred spectra assuming the modified Gaussian shape. The corresponding E_o profiles were previously presented in the upper two panels of Figure 20. We observe a lowering of $h_{max}E$ by more than 5 km for an inferred E_o based on full MSIS O density compared to one based on half of this density. This is simply a reflection of the sensitivity of E_o to O using 1356/3914 data as presented in the upper panel of Figure 20.

The dotted curve in each panel is based on inferred spectra assuming the modified Maxwellian shape. The corresponding E_o profile was previously shown in the lower panel of Figure 20 (solid curve). The Maxwellian based curves should be compared to the solid curves to see just the effect of assuming a Maxwellian instead of a Gaussian shape for the incident electron spectrum. The $h_{max}E$ curve for Maxwellians lies above that for Gaussians which is as expected due to a broader distribution of energies in the former spectrum. For this same reason $N_{max}E$ for the inferred Maxwellians lies below that for the corresponding Gaussians.

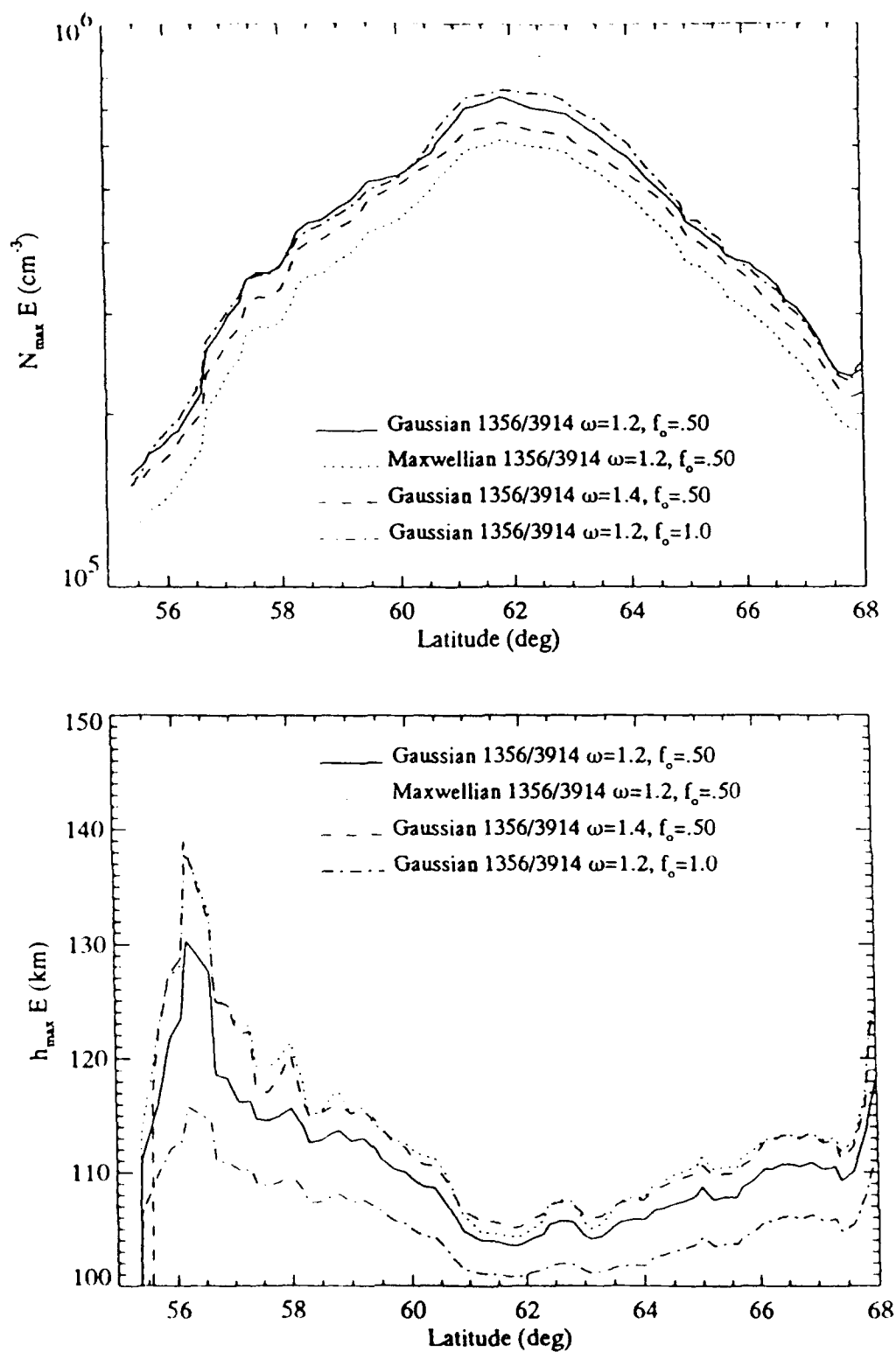The amount of spread in $h_{max}E$ cannot be equated to its uncertainty. An important part

Fig. 24   E-layer electron density parameters $N_{max}E$ and $h_{max}E$ versus latitude for the Jan 29 pass. The results are based on E_0 and Q profiles using the 21 pixel averaged 1356/3914 data ratio in Figure 15 and various pairs of 1356 Å and 3914 Å yields identified in the figure

of this spread comes from the use of 1356 Å data and their interpretation in terms of two O densities taken to be a factor of two apart. More will be said on this subject in the next section when discussing anticipated improvements using data from future experiments involving spectrographs.

The altitude $h_{max}E$ is seen to range from about 105 to 120 km excluding the spike at about 56.5°. This is expected based on comments in the previous section concerning the expected range in E_0. Further discussion of the overall behavior of $h_{max}E$ will follow in the next section.

8.2   Jan 12 pass

Figure 25 shows results similar to those in Figure 24 except for the Jan 12 pass wavelengths 1304 Å and 3914 Å. Again, results using LBH data (specifically, the 1544/3914 data ratio) are not shown because of problems discussed in the previous section. Larger $h_{max}E$ values occur on this pass reflecting the smaller inferred E_0 values. Considerable sensitivity to O exists which reflects the sensitivity of E_0 to O using the 1304/3914 data ratio. Similar to 1356 Å, this argues against use of 1304 Å data for inferring spectral hardness unless the O density is known. On the other hand, such data are valuable for monitoring O if spectral hardness can be estimated from other data such as LBH data. This is discussed further in the next section.
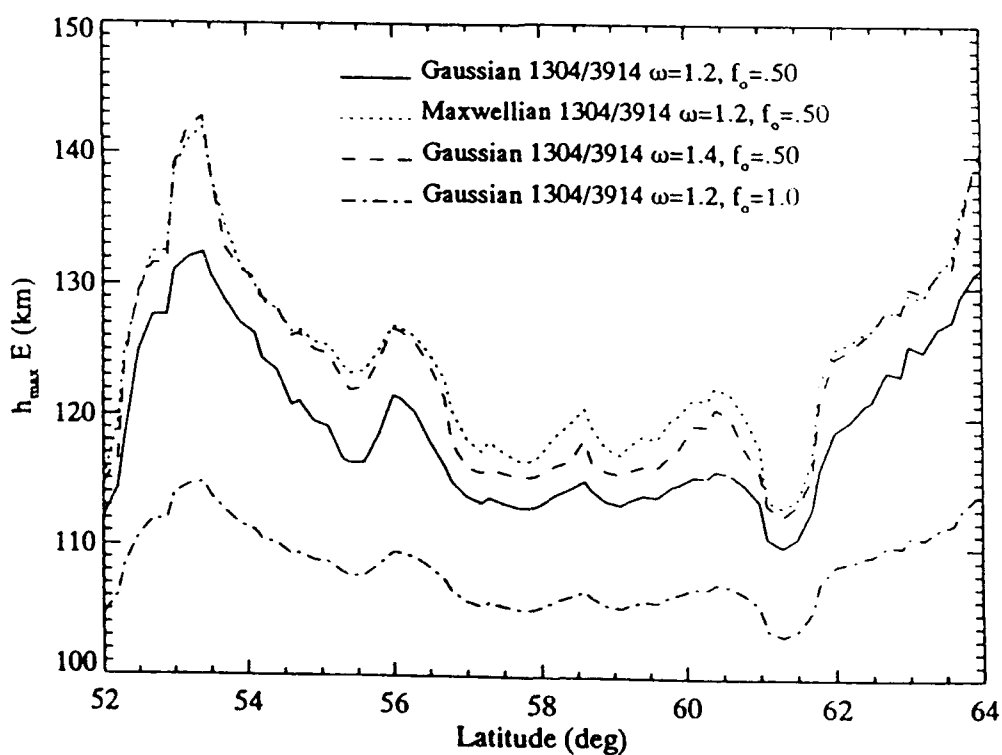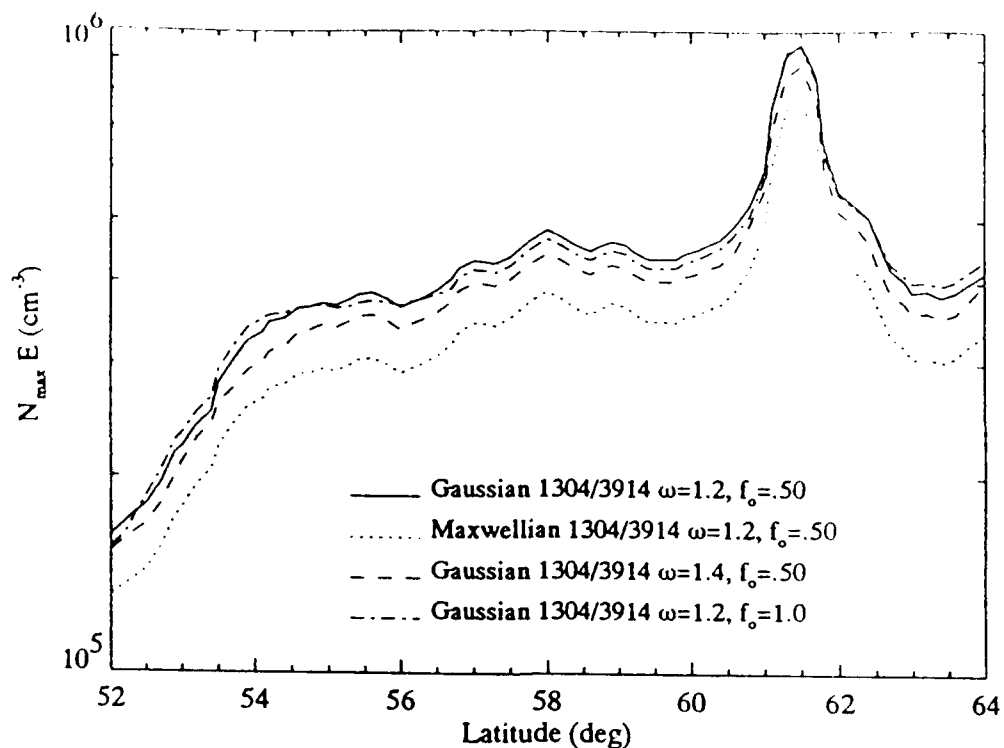
Fig. 25   Similar to Figure 24 except for the Jan 12 pass using the 21 pixel averaged
1304/3914 data ratio in Figure 17

9. DISCUSSION AND CONCLUSIONS

A clear correlation is present between the latitudinal profiles of E_o and Q for both passes. For example, on the Jan 29 pass, as Q increases from about 5 to 20 ergs $cm^{-2}s^{-1}$ in Figure 18 (58° to 62°), E_o increases from about 4 to 10 keV in Figure 19. On the Jan 12 pass, we observe strongly correlated structure between Q and E_o in the region of high energy deposition (61°). Correlation is also present over much of remaining range of latitudes. This suggests that much of the emission recorded along the chosen cuts through the images from these passes was produced at least in part by discrete aurora. It is likely that an extended latitudinal region of discrete aurora was embedded in diffuse aurora. Christensen et al. (1987) reported on the correlation of Q with E_o using ground based optical data (OI 6300 Å and N_2^+ 1N 4278 Å) and interpreted the correlation in terms of discrete aurora in which precipitating electrons have been accelerated through electrostatic potentials. They refer to the theoretical work of Knight (1973) and Lyons (1981) who examined the spectral characteristics of plasma sheet electron distributions after passing through acceleration regions several thousand kilometers above the ionosphere.

In work as yet unpublished, Strickland et al. (1992) also observe good Q, E_o correlation based on Sondrestrom radar data in the form of EDPs. An extensive set of Q and E_o values was obtained by carefully fitting model EDPs to data from several events. Some data were best fitted using model EDPs based on incident electron spectra characterized by modified Maxwellian distributions while others required modified Gaussian distributions. Poor correlation between Q and E_o was observed for Maxwellian results whereas good correlation was observed for Gaussian results. This confirms the notion that precipitating electrons possessing Gaussian-like distributions have undergone acceleration as discussed in the above referenced papers.

As already discussed, we are not able to provide a single latitudinal profile of E_o with error bars for a selected cut through the images. Using 1356/3914 data, e.g., this would require knowledge of the abundance of O relative to N_2 and the 3914 Å albedo along the cut. We eliminate the problem of not knowing O by using LBH/3914 data if enough counts are available for the observed LBH bands. This was not the case in this analysis as indicated by the large

statistical fluctuations in the results based on LBH data. Significant improvement in the accuracy of E_o and Q should occur on future experiments such as SSUSI to be flown on DMSP where much better spectral information will be obtained using spectrographs. Provided good counting statistics are available, E_o and Q can be obtained using the fully observed LBH spectrum from the spectral region of strongest O_2 absorption (near 1400 Å) to weak absorption (near the beyond 1700 Å). This eliminates problems associated with the O concentration and albedo. Knowing E_o and Q, 1356/LBH or 1304/LBH data will then determine the O concentration. Some small degree of error is expected in the LBH derived E_o due to error in the initially applied O density. This error in E_o should be effectively eliminated in one iteration, however, using the derived O density. Some error in E_o is also expected from uncertainty in the applied O_2 density relative to that of N_2. While this problem will need to be examined, we do not anticipate serious error from this uncertainty.

In summary, we have presented a first analysis in which precipitating electron spectral characteristics over an extended latitudinal region of the auroral zone have been obtained using satellite observed FUV emissions along with emission from the N_2^+ 1N system at 3914 Å. While we are unable to state the accuracy of the derived E_o profiles due to limitations within the present data set, evidence has been presented that overall magnitude and relative variation of E_o with latitude are within expectations based on satellite and rocket particle data collected over the past three decades. The findings of this analysis offer encouragement to the use of FUV auroral data from future satellite spectrographic experiments for monitoring E-region EDP*s* and associated conductivities along with the abundance of O relative to that of N_2.

10. REFERENCES

Ajello, J. A., Dissociative excitation of O_2 in the vacuum ultraviolet by electron impact, *J. Chem. Phys.*, *55*, 3156, 1971.

Ajello, J. M. and D. E. Shemansky, A Re-examination of Important N_2 Cross Sections by Electron Impact with Application to the Dayglow: The Lyman-Birge-Hopfield Band System and NI (119.99 nm), *J. Geophys. Res.*, *90*, 9845, 1985.

Arnoldy, R. L., P. B. Lewis, and P. O. Isaacson, Field-aligned auroral electron fluxes, *J. Geophys. Res.*, *79*, 4208, 1974.

Bingham, R. D., D. A. Bryant, and D. S. Hall, Auroral acceleration by lower-hybrid waves, *Ann. Geophys.*, *6*, 159, 1988.

Borst, W. L. and E. C. Zipf, Cross Section for Electron-Impact Excitation of the (0,0) First Negative Band of N_2^+ from Threshold to 3 keV, *Phys. Rev. A*, *1*, 834, 1970.

Bryant, D. A., Wave acceleration of auroral electrons, ESA Scientific Publication SP-270, 273, 1987.

Burch, J. L., Diagnosis of auroral acceleration mechanism by particle measurements, Auroral Physics, ed. C.-I. Meng, M. J. Rycroft, and L. A. Frank, Cambridge UP, p. 97, 1991.

Christensen, A. B., L. R. Lyons, J. H. Hecht, G. G. Sivjee, R. R. Meier and D. J. Strickland, "Magnetic Field-Aligned Electric Field Acceleration and the Characteristics of the Optical Aurora", *J. Geophys. Res.*, *92*, 6163, 1987.

Chui, Y. T. and M. Schulz, Self consistent particle and parallel electrostatic field distributions in the magnetospheric-ionospheric auroral region, *J. Geophys. Res.*, *83*, 629, 1978.

Chui, Y. T., J. M. Cornwall, J. F. Fennell, D. J. Gorney, and P. F. Mizera, Auroral plasmas in the evening sector: satellite observations and theoretical interpretations, *Space Sci. Rev.*, *35*, 211, 1983.

DelGreco, F. P., R. E. Huffman, J. C. Larrabee, R. W. Eastes, F. J. LeBlanc, and C.-I. Meng, Organizing and utilizing the imagery and spectral data from Polar BEAR, *Ultraviolet Technology II*, R. E. Huffman, Editor, *Proc. SPIE*, *932*, 30, 1988.

Erdman, P. W., and E. C. Zipf, Excitation of the OI ($3s^5S^o$ - $3p^5P$; $\lambda7774$ Å) multiplet by electron impact on O_2, *J. Chem. Phys.*, *87*, 4540, 1987.

Evans, D. S., Precipitating electron fluxes formed by a magnetic field aligned potential difference, *J. Geophys. Res.*, *79*, 2853, 1974.

Frank, L. A., and K. L. Ackerson, Observations of charged particle precipitation into the auroral zone, *J. Geophys. Res.*, *76*, 3612, 1971.

Germany, G. A., M. R. Torr, P. G. Richards, and D. G. Torr, The dependence of modeled OI 1356 and N_2 Lyman Birge Hopfield auroral emissions on the neutral atmosphere, *J. Geophys. Res.*, *95*, 7725, 1990.

Hardy, D. A., M. S. Gussenhoven, and E. Holeman, A statistical model of auroral electron precipitation, *J. Geophys. Res.*, *90*, 4229, 1985.

Hardy, D. A., M. S. Gussenhoven, and D. Brautigam, A statistical model of auroral ion precipitation, *J. Geophys. Res.*, *94*, 370, 1989.

Hecht, J. H., D. J. Strickland, A. B. Christensen, D. C. Kayser, and R. L. Walterscheid, Lower Thermospheric Composition Changes Derived from Optical and Radar Data Taken at Sondre Stromfjord During the Great Magnetic Storm of February, 1986, *J. Geophys. Res.*, *96*, 5757,

1991.

Hedin, A. E., MSIS-86 Thermospheric Model, *J. Geophys, Res.*, *92*, 4649, 1987.

Huffman, R. F., F. J. LeBlanc, J. C. Larrabee, and D. E. Paulsen, Satellite vacuum ultraviolet airglow and auroral observations, *J. Geophys. Res.*, *85*, 2201-2215, 1980.

Knight, S., Parallel electric fields, *Planet. Space Sci.*, *21*, 741, 1973.

Lin, C. S. and R.A. Hoffman, Characteristic of the inverted-V event, *J. Geophys. Res.*, *84*, 1514, 1979a.

Lin, C. S. and R.A. Hoffman, Fluctuations of inverted-V electron fluxes, *J. Geophys. Res.*, *84*, 6547, 1979b.

Lin, C. S. and R. A. Hoffman, Observations of inverted-V electron precipitation, *Space Sci. Rev.*, *33*, 415, 1982.

Lyons, L. R., Discrete aurora as the direct result of an inferred high altitude generating potential distribution, *J. Geophys. Res.*, *86*, 1, 1981.

Lyons, L. R., D. S. Evans, and R. Lundin, An Observed Relation Between Magnetic Field-Aligned Electric Fields and Downward Electron Energy Fluxes in the Vicinity of Auroral Forms, *J. Geophys. Res.*, *84*, 457, 1979.

McFadden, J. P., C. W. Carlson, M. H. Boehm, and T. J. Hallinan, Field-aligned electron flux oscillations that produce flickering aurora, *J. Geophys. Res.*, *92*, 11133, 1987.

McFadden, J. P., C. W. Carlson, and M. H. Boehm, Structure of an energetic narrow discrete arc, *J. Geophys. Res.*, *95*, 6533, 1990.

Meier, R. R., D. J. Strickland, J. H. Hecht and A. B. Christensen, Deducing composition and incident electron spectra from ground-based auroral optical measurements: A study of auroral red line processes", *J. Geophys. Res.*, *94*, 13541, 1989.

Meier, R. R., Ultraviolet spectroscopy of remote sensing of the upper atmosphere, *Space Sci. Rev.*, *58*, 1, 1991.

Reiff, P. H, H. L. Collin, J. D. Craven, J. L. Burch, J. D. Winningham, E. G. Shelley, L. A. Frank, and M. A. Friedman, Determination of auroral electrostatic potentials using high- and low-altitude particle distributions, *J. Geophys. Res.*, *93*, 7441, 1988.

Robinson, R., T. Dabbs, J. Vickrey, R. Eastes, F. Del Greco, R. Huffman, C. Meng, R. Daniell, D. Strickland, and R. Vondrak, Coordinated Measurements made by the Sondrestrom Radar and the Polar BEAR Ultraviolet Imager, *J. Geophys. Res.*, *97*, 2863, 1991.

Schenkel, F. W., B. S. Ogorzalek, J. C. Larrabee, F. J. LeBlanc, and R. E. Huffman, Ultraviolet daytime auroral and ionospheric imaging from space, *Applied Optics*, *24*, 3395-3405, 1985.

Schenkel, F. W., B. S. Ogorzalek, R. R. Gardner, R. A. Hutchins, R. E. Huffman, and J. C. Larrabee, Simultaneous multispectral narrow band auroral imagery from space (1150 Å to 6300 Å), *Ultraviolet Technology*, R. E. Huffman, Editor, *Proc. SPIE*, *687*, 90, 1986.

Schumaker, T. L., M. S. Gussenhoven, D. A. Hardy, and R.L. Carovillano, The relationship between diffuse auroral and plasma sheet electron distributions near local midnight, *J. Geophys. Res.*, *94*, 10061, 1989.

Sharber, J. R., The continuous (diffuse) aurora and auroral-E ionization, in Physics of Space Plasmas, 7, ed. T. S. Chang, B. Coppi, and J. R. Jasperse, p. 115, Scientific Publishers, Cambridge, MA, 1981.

Stone, E. J. and E. C. Zipf, Electron Impact Excitation of the ^3S and ^5S States of Atomic Oxygen, *J. Chem. Phys.*, *60*, 4237, 1974.

Strickland, D. J., D. L. Book, T. P. Coffey and J. A. Fedder, Transport Equation Techniques for the Deposition of Auroral Electrons, *J. Geophys. Res.*, *81*, 2755, 1976.

Strickland, D. J., J. R. Jasperse and J. A. Whalen, Dependence of Auroral FUV Emission on the Incident Electron Spectrum and Neutral Atmosphere, *J. Geophys. Res.*, *88*, 8051, 1983.

Strickland, D. J., and D. E. Anderson, Jr., Radiation transport effects on the OI 1356 Å limb intensity profile in the dayglow, *J. Geophys. Res.*, *88*, 9260, 1983.

Strickland, D. J., R. R. Meier, J. H. Hecht and A. B. Christensen, Deducing Composition and Incident Electron Spectra from Ground-Based Auroral Optical Measurements: Theory and Model Results, *J. Geophys. Res.*, *94*, 13527, 1989.

Strickland, D. J., B. Basu, J. R. Jasperse, and R. E. Daniell, A Linear Transport Theory for the Electron-Proton-Hydrogen Atom Aurora, submitted to *J. Geophys. Res.*, 1991.

Strickland, D. J., J. H. Hecht, R. Link, and A. B. Christensen, The Relationship Between Energy Flux Q and Mean Energy <E> of Auroral Electron Spectra Based on Radar Data from the 1987 CEDAR Campaign at Sondre Stromfjord, Greenland, to be submitted to *J. Geophys. Res.*, 1992.

Temerin, M., J. McFadden, M. Boehm, C. W. Carlson, and W. Lotko, Production of flickering aurora and field-aligned electron flux by electromagnetic ion cyclotron waves, *J. Geophys. Res.*, *91*, 5769, 1986.

Vallance Jones, A., Aurora, D. Reidel, Hingham, MA, 1974.

Wells, W. C., W. L. Borst, and E. C. Zipf, Absolute Cross Section for the Production of $O(^5S^0)$

by Electron Impact Dissociation of O_2, *Chem. Phys. Lett.*, *12*, 288, 1971.

Zipf, E. C. and P. W. Erdman, Electron Impact Excitation of Atomic Oxygen: Revised Cross Sections, *J. Geophys. Res.*, *90*, 11087, 1985.